NOAA Technical Memorandum NESDIS AISC 7

APPLICATION OF AVHRR SATELLITE DATA TO THE STUDY OF SEDIMENT AND CHLOROPHYLL IN TURBID COASTAL WATER

Richard P. Stumpf

Washington, D.C.
March 1987

U.S. DEPARTMENT OF COMMERCE / National Oceanic and Atmospheric Administration / National Environmental Satellite, Data, and Information Service

NOAA TECHNICAL MEMORANDUMS

National Environmental Satellite Data and Information Services,
Assessment and Information Services Center Subseries

The Assessment and Information Services Center provides value-added environmental information to support national needs and goals. The products and services of AISC's staff of environmental scientists, economists, librarians and information specialists, and computer specialists provide decision assistance to the nation's resource managers. AISC's programs in environmental assessments and environmental information management complement the data collection and archival program of other National Environmental Satellite Data and Information Services (NESDIS) components.

The Technical Memorandum series provides an informal medium for the documentation and quick dissemination of results not appropriate, or not yet ready, for formal publication in the standard journals. The series is used to report on work in progress, to describe technical procedures and practices, or to report to a limited audience.

These papers are available from the originating office and also from the National Technical Information Service (NTIS), U.S. Department of Commerce, 5285 Port Royal Road, Springfield, VA 22151. Prices vary for paper copy and microfiche.

NESDIS Technical Memorandum

AISC 1 Assessment Models for Surface Dispersion of Marine Pollutants. Kurt W. Hess, Fred G. Everdale, and Peter L. Grose, May 1985.

AISC 2 Comparison of Boundary Layer Winds from NWS LFM Output and Instrumented Buoys. Robert W. Reeves, and Peter J. Pytlowany, May 1985.

AISC 3 Assessments Model for Estuarine Circulation and Salinity, Kurt W. Hess, June 1985.

AISC 4 Development of a Tropical Cyclone Damage Assessment Methodology. Isobel C. Sheifer and John O. Ellis, January 1986.

AISC 5 Interdisciplinary Synoptic Assessment of Chesapeake Bay and the Adjacent Shelf. Edited by David F. Johnson, Kurt W. Hess, and Peter J. Pytlowany, August 1986.

AISC 6 Numerical Model of Circulation in Chesapeake Bay and the Continental Shelf. Kurt W. Hess, November 1986.

NOAA Technical Memorandum NESDIS AISC 7

APPLICATION OF AVHRR SATELLITE DATA TO THE STUDY OF SEDIMENT AND CHLOROPHYLL IN TURBID COASTAL WATER

Richard P. Stumpf

Marine Environmental Assessment Division
Assessment and Information Services Center

Washington, D.C.
March 1987

UNITED STATES
DEPARTMENT OF COMMERCE
Malcolm Baldrige,
Secretary

National Oceanic and
Atmospheric Administration
Anthony J. Calio,
Under Secretary

National Environmental Satellite,
Data, and Information Service
Thomas N. Pyke, Jr.
Assistant Administrator

CONTENTS

APPLICATION OF AVHRR SATELLITE DATA TO THE STUDY OF SEDIMENT AND CHLOROPHYLL IN TURBID COASTAL WATER

Richard P. Stumpf

Marine Environmental Assessment Division
Assessment and Information Services Center
National Environmental Satellite, Data, and
Information Service, Washington, D.C. 20235

ABSTRACT. Newly developed algorithms permit reliable estimates of chlorophyll and suspended sediment content of estuarine and coastal waters using data collected from satellite. These algorithms include correction for atmospheric effects and calculation of reflectance, thereby allowing interscene comparison and even comparison of data collected with different sensors.

Satellite measurement of sediment concentration may be as accurate as ±30% in regions of constant and uniform sediment grain size. Grain size variation produces a systematic variation in reflectance. In many cases sunglint and some haze can be eliminated from the imagery, improving the imagery for estimating sediment concentration. Chlorophyll content in estuaries can be related to water color measured using only red and near-infrared light. Concentrations of chlorophyll may be estimated to within ±60%, with the greatest error due to atmospheric contamination.

The Advanced Very High Resolution Radiometer (AVHRR) satellite sensor, already used to determine sea surface temperatures, has the sensitivity and dynamic range to provide usable data on sediment and chlorophyll for estuaries having a wide range in turbidity. The satellite also has an overpass frequency of 12 hours, and two daytime overpasses when two satellites are operating. For many larger estuaries (>100 km^2), the AVHRR could improve analysis of processes and improve model verification.

1. INTRODUCTION

Estuarine and other turbid coastal waters have become the subject of much interest and research in recent years. Most of the investigations of these areas have been driven by concern over water quality and the effects of pollution on fisheries and recreational use. Modeling and monitoring programs have been established to try to determine distributions and dispersion of various materials. These programs, in turn, require large

quantities of data and extensive sampling programs owing to the enormous temporal and spatial variability of coastal waters.

Both circulation patterns and the sediment and nutrient loads vary rapidly in estuaries, depending on numerous factors such as the local river discharge, the local wind field, the bathymetry and the presence of water mass fronts. This variability makes the study of estuaries from in situ measurements quite difficult. Shipboard sampling cannot affordably provide the synoptic data and temporal detail needed to study many estuarine processes and materials. However, satellites, which have routine, synoptic coverage, offer a means of obtaining some of the necessary data.

Satellite remote sensing has greatly enhanced our knowledge of the open ocean. Satellites can now provide accurate data on sea surface temperature (Strong and McClain, 1984) and elevation (Born et al., 1984), and they have been shown capable of providing good estimates of oceanic chlorophyll and biomass (Gordon et al., 1983). Frequent collection of this information has begun to allow oceanographers to study various physical and biological processes in the ocean.

In turbid coastal and estuarine waters, remote sensing has not had such successes. The effectiveness of the Coastal Zone Color Scanner (CZCS), which is used to determine oceanic chlorophyll, is limited by turbidity. The algorithms have been pushed to work in slightly turbid water (Tassan and Sturm, 1986), but in moderately turbid water, not only do the oceanic algorithms break down, but the high reflectance saturates the sensor. Landsat and SPOT (Systeme Probataire d'Observation de la Terre), on the other hand, have the dynamic range to study turbid water, but lack the overpass frequency needed to examine estuarine dynamics. Most estuarine processes occur on daily or weekly time scales, far too short for study using monthly imagery. Statistical analyses of fifteen years of Landsat data has been used to infer some estuarine processes (Munday and Fedosh, 1981), but direct time series analysis of events is rarely possible (for an exception see Stumpf, 1987).

Landsat's poor temporal resolution has also limited the development of general algorithms to measure both sediment and chlorophyll. Munday and Alfoldi (1979) have had some success with a technique for estimating sediment concentration, and Stumpf (1985) has detected variations in sediment and water color. However, most relationships between Landsat data and in situ data are limited to specific data sets (Catts et al., 1985; Bowker et al., 1975) and are not general enough to be applied elsewhere.

The NOAA Advanced Very High Resolution Radiometer (AVHRR), which is known in oceanography almost exclusively for providing sea surface temperature maps, may offer a means of studying

estuaries (Table 1). It provides frequent routine coverage of the globe, potentially two daytime images each day when two satellites are operating as at present. It has the sensitivity to distinguish variability in moderately turbid water and it has the dynamic range (i.e., saturation radiance) to study even the most turbid waters (Gagliardini et al., 1982). The poor spatial resolution of the sensor is a disadvantage only when considering fine-scale structure or small estuaries. The red and near-infrared bands, the two reflected bands found on the AVHRR, are well suited for research in turbid water, as shall be presented, and they have corresponding bands on other sensors (Table 2).

This paper will first develop general algorithms to estimate suspended sediment and chlorophyll content of turbid water from satellite. These algorithms will allow some comparison of different estuaries and different conditions, and can be used with different satellites. It will then show the specific application of the algorithms to the AVHRR, and the sensor's potential application to the study of dynamic turbid waters.

Table 1. Comparison of Sensor Characteristics

	AVHRR	MSS	TM	SPOT	CZCS[1]
resolution (km)	1.1	.08	.03	.02	.82
frequency (days)	0.5-1	16	16	26[2]	3-5
scene width (km)	2000	180	180	60	1500
# of bands					
reflected	2	4	4	3	5
thermal	3	0	2	0	1
radiometric resolution per count					
red band	.052	.131	.081	.040	.005
near-IR band	.034	.115	.084	.055	.093
($mW\text{-}cm^{-2}\mu m^{-1}sr^{-1}$)					
saturation radiance					
red band	50.	17.9	20.4	10.2	2.9
near-IR band	33.	14.8	20.6	14.0	23.9
($mW\text{-}cm^{-2}\mu m^{-1}sr^{-1}$)					

[1]The CZCS was turned off in 1986 with no plans for a replacement.

[2]The SPOT sensor can be pointed upon request, therefore, an area can be imaged several times during a cycle.

Table 2. Red and Near-Infrared Bands

	AVHRR	MSS	TM	SPOT	CZCS
Red (nm)	580-680	600-700	630-690	610-680	660-680
band #	1	5 or 2	3	2	4
Near-IR (nm)	720-1000	700-800	760-900	790-890	700-800
band #	2	6 or 3	4	3	5

2. ADVANCED VERY HIGH RESOLUTION RADIOMETER

The AVHRR is on the polar-orbiting sun-synchronous NOAA TIROS (Television and Infrared Observation Satellite) satellite platform. The orbit is oriented north-south and the satellite track progresses with the sun so that images at the same latitude are taken at the same local solar time. For NOAA-6,8,and 10, daytime overpasses occur about 0800 local time; for NOAA-7 and 9, they occur about 1400 local time. The afternoon passes are generally superior in quality owing to the greater illumination by the high afternoon sun, but morning passes over mid-latitudes often have sufficient illumination during the spring and summer to be used. The satellites have approximately a 9-day cycle and track from west to east. Hence an image area will appear on the east side of an image on the first day, and on the following days move progressively to nadir, then to the west side of the image. After 9 days, the area will appear back on the east side of the image and a new cycle starts.

There are five bands on the AVHRR as shown in Table 3. Channels 3,4, and 5 are used to calculate sea surface temperature, using algorithms as presented in Strong and McClain (1984) and McMillan and Crosby (1984). Channels 1 and 2 have been used primarily for the study of vegetation and crops, viewing ice and snow cover, and for monitoring cloud cover and weather.

The sensor scans from right to left in a line orthgonal to the direction of travel. The instantaneous field of view is 1.4 milliradians (1.1 km) and the pixel size is about 0.8 km (along line) x 1.1 km (across line). A scanline includes 2048 pixels, covering an angle of $\pm 55.4^{o}$ from nadir. The satellite collects 360 scanlines per minute.

The specifications of the AVHRR are described in detail in Kidwell (1984) and Lauritson et al. (1979). Example treatment and some applications of the data to oceanography are presented in Everdale (1986).

Table 3. AVHRR Spectral Bands

channel	1	2	3	4	5
wavelength (μm)	.58-.68	.72-1.0	3.5-3.9	10.5-11.3	11.5-12.5
description	red	near-IR	t h e r m a l - i n f r a r e d		

3. OPTICAL REMOTE SENSING OF THE OCEAN

3.1. General Principles

In order to understand the application of satellite data to the study of the water column, we should define some basic terms. Details of marine optics and optical remote sensing can be found in texts such as Jerlov (1976) or Gordon and Morel (1981).

Reflectance (R) is defined as

$$R(\lambda) = E_u(\lambda)/E_d(\lambda) \qquad (3.1)$$

where λ is the spectral band or wavelength. E_u is the upwelling irradiance, and E_d is the downwelling irradiance. Irradiance is the energy per unit area passing through a surface. Generally E_d is estimated as the solar constant corrected for the sun's altitude and the distance from the earth to the sun:

$$E_d(\lambda) = E_o(\lambda)\ \cos\theta_o \qquad (3.2)$$

where E_o is the solar constant, with $E_o = \underline{E}_o[1-.0167\cos(D-3)]^2$, $\underline{E}_o$ = the mean solar constant, D = the Julian date (day of the year), and θ_o is the solar zenith angle ($90 - \theta_o$ equals the sun's altitude angle).

A satellite actually detects radiance, namely that portion of the irradiance that is directed toward the sensor. Radiance (L) is defined as the energy per unit area per solid angle in a specific direction that passes a surface. Irradiance and radiance can be related through

$$E(\lambda) = \int_{\Omega} L(\lambda,\Omega)\, d\Omega \qquad (3.3a)$$

or

$$E(\lambda) = 2\pi \int_{0}^{\pi/2} L(\lambda,\theta)\cos\theta\, d\theta \qquad (3.3b).$$

where $d\Omega$ is an element of solid angle, θ is an angle from the surface normal. In (3.3b), L is constant at each θ.

For remote sensing, the upwelling irradiance, E_u, is equated to the upwelling radiance from the water, L_w, measured by the sensor through

$$E_u(\lambda) = Q(\lambda)\, L_w(\lambda) \qquad (3.4)$$

where Q is a constant of proportionality defined by (3.4), which would result from solving (3.3). If the radiant field is completely diffuse, so that L is constant with angle θ, then by solving (3.3b) we find that $Q = \pi$. This fixed value for Q is commonly used in remote sensing, although Q has been measured to have values between π and 5, and may vary with wavelength (Austin, 1979).

The satellite detects the combined radiance of the water column, the water surface, and the atmosphere (Figure 1). The detected radiance can be expressed as

$$L_*(\lambda) = T(\lambda)L_w(\lambda) + T(\lambda)L_g(\lambda) + L_A(\lambda) \qquad (3.5)$$

where L_* is the radiance detected by the satellite, L_w is the radiance leaving the water column, L_g is the radiance reflected from the water surface (i.e., sunglint), L_A is the radiance from the atmosphere, referred to as path radiance, and T is the atmospheric transmission coefficient.

In (3.5) we are interested in L_w in order to determine the water reflectance. From equations (3.1), (3.2), and (3.4), we can see that L_w depends on both the reflectance of the water and the incident sunlight, namely:

$$L_w(\lambda) = R(\lambda)\, E_o(\lambda)\cos\theta_o \,/\, Q \qquad (3.6)$$

In (3.6), E_o is constant at any given wavelength and Q is presumed constant for all wavelengths. R is dependent only on the materials in the water. Therefore in order to reliably and consistently determine the characteristics of the water column and the materials within it, we must obtain R by correcting for sunglint, L_g, atmospheric effects L_A and T, and the solar zenith angle θ_o.

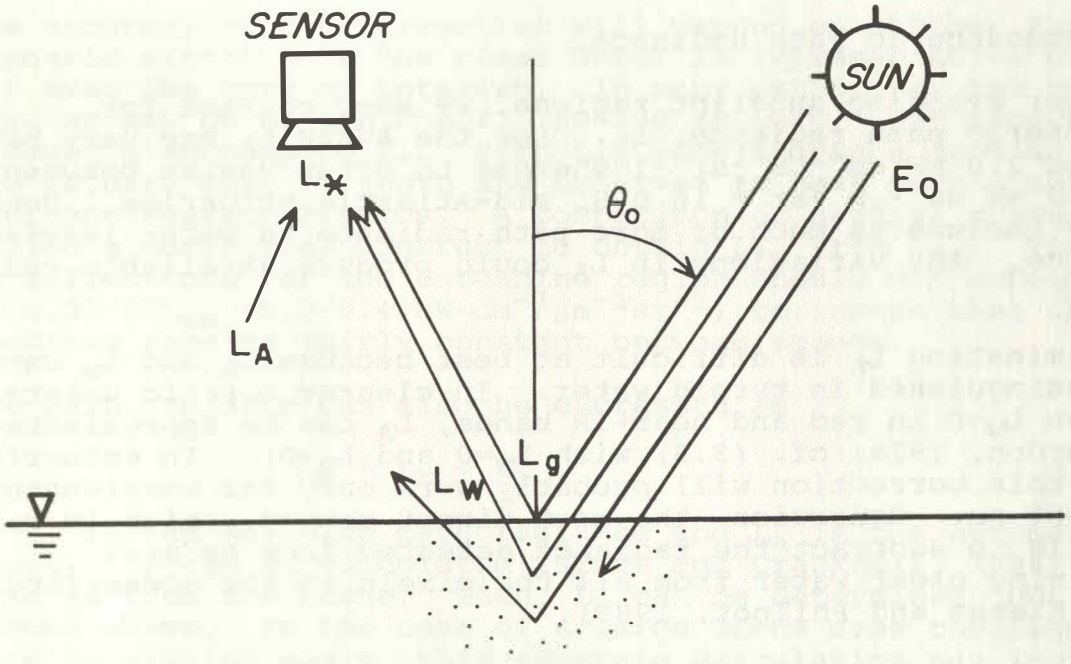

Figure 1: Sources of radiance observed at the satellite

3.2. Sunglint.

Surface reflection is the specular reflection directly off the water's surface. The skylight reflected back to the sensor is negligible, generally less than 0.2% of the sunlight (Philpot, 1981). However, reflected sunlight, or sunglint, can be substantial, up to 6% of the incident sunlight.

The intensity of sunglint varies with the surface wave field, therefore it depends on surface winds, currents, and bathymetry. As a result, it will vary considerably throughout a scene, and cannot be adequately approximated. Therefore, the simplest solution to the sunglint problem is to avoid regions containing sunglint. With a wide angle scanner, such as the AVHRR, the image half opposite the sun will always be free of sunglint. For afternoon passes, the eastern half to two-thirds will not contain

any sunglint, for morning passes the western portion will be free. In mid-latitudes during the fall and winter, the afternoon passes generally produce images completely free of sunglint owing to the low solar altitude. For certain applications, the sunglint can be removed. This technique will be described in detail in chapter 6.

3.3. Atmospheric Path Radiance.

After avoiding sunglint regions, we must correct for atmospheric path radiance, L_A. For the AVHRR L_A may vary between 1.0 and 2.0 mW $cm^{-2}\mu m^{-1}sr^{-1}$, whereas L_w often varies between 0.2 and 3.0 mW $cm^{-2}\mu m^{-1}sr^{-1}$ in U.S. mid-Atlantic estuaries. Hence, L_* may include as much or more path radiance as water leaving radiance. Any variations in L_A could produce unreliable results in L_w.

Eliminating L_A is difficult at best because L_A and L_w cannot be distinguished in turbid water. In clearer oceanic waters, because L_w=0 in red and near-IR bands, L_A can be approximated as L_* (Gordon, 1978; cf. (3.5) with L_w=0 and L_g=0). In estuarine water this correction will probably work only for wavelengths for 100-2000 nm. Otherwise, the most direct method, which is used here, is to subtract the radiance detected from an area containing clear water from all the pixels in the scene (Sturm, 1981; Klemas and Philpot, 1983).

Clearwater is defined here as water which has a radiance, L_w, equivalent to 0-2 counts for the sensor; thus it depends to a degree on the sensor band's sensitivity (Table 1). For example, clearwater for the AVHRR is much clearer than for the MSS; and CZCS red band would have the clearest water. If L_w is negligible, then (3.5) reduces to

$$L_{Ac}(\lambda) = L_{*c}(\lambda) \qquad (3.7)$$

with L_{*c} being the lowest value of L_* for clearwater in the scene and L_{Ac} being the atmospheric correction that is subtracted from all values of L_*.

This method of correcting for path radiance, the "clearwater subtraction technique", assumes that L_A is constant over the whole study area. Taking the lowest value of L_{*c}, means that L_{Ac} will be a minimum estimate. The error resulting from this assumption will tend to increase with the size of the study area owing to the tendency for greater atmospheric variability over larger areas. The error will especially increase with the viewing angle of the satellite because the atmospheric path length and, therefore, L_A vary with the secant of the viewing angle. If a wide range of view angles is contained in the image, such as along east-west trending shorelines, the correction at

each pixel, i, could be determined as

$$L_A(i) = L_{Ac} \sec \theta_v(i)/\sec \theta_v(i_c) \qquad (3.8)$$

where $\theta_v(i)$ is the viewing angle to pixel i and $\theta_v(i_c)$ is the viewing angle for the clearwater pixel (Durkee et al., 1986).

The accuracy of the correction will depend on whether the atmospheric signal over the clear water is representative of the signal over the area of interest. In many estuaries, the nearest clearwater may be on the shelf, 100-300 km away. Our recourse in this case is to compare L_{*c} with L_{*e}, the radiance from an area in the estuary that is known and observed to have very stable reflectance characteristics. A comparison of several scenes can establish a correction constant to obtain L_{*c} from L_{*e}. The red light reflectance for the estuarine region should not exceed about 0.01 (TL_{we} <0.2-0.4 mW-cm$^{-1}\mu$m^{-1}sr^{-1}) to insure that the reflectance remains fairly constant between scenes.

The path radiance can also be expressed as

$$L_A = L_r + L_a \qquad (3.9)$$

where L_r is the Rayleigh path radiance and L_a is the aerosol path radiance. L_r can be calculated (Singh and Cracknell, 1986) and subtracted from the scene. Then, L_a can be determined just as L_A was found above. In the case of a large scene area covering 20^o or more in viewing angle, this separate calculation may improve results across the scene if L_a is corrected using the form of (3.8), otherwise, using L_A alone is satisfactory.

3.4. Atmospheric Attenuation.

Eliminating the sunglint and path radiance, we can rewrite (3.5) as

$$T\, L_W = L_* - L_{Ac} \qquad (3.10)$$

for each spectral band, and L_{Ac} is determined using 3.7 or, alternatively, either (3.8) or (3.9). The transmission coefficient, T, is defined as

$$T = \exp(-t/\cos \theta_v) \qquad (3.11)$$

The optical depth, t, can be expressed as

$$t = t_r - t_a \qquad (3.12)$$

The Rayleigh optical depth, t_r, is a constant. The aerosol optical depth, t_a, has been shown to vary linearly with L_a, the aerosol path radiance. Although L_r, the Rayleigh path radiance,

tends to vary somewhat with the viewing and sun geometry, Ahern et al. (1977) have shown a strong linear relation between L_A and t. Based on that work and values of path radiance and T reported in Durkee (1984), Austin (1979), and Griggs (1983), t is estimated from L_{Ac} as

$$t_1 = 0.09 + 0.03(L_{Ac1} - 0.80) \qquad (3.13)$$

$$t_2 = 0.05 + 0.04(L_{Ac2} - 0.20)$$

where subscripts 1 and 2 denote AVHRR channels 1 and 2. The accuracy of t cos θ_v and, therefore, T is within $\pm$5%. We should note that attenuation is not a major source of error; interscene comparisons of L_w will, in general, be improved only 0-20% by correcting for T. When T becomes much smaller than 0.7, the variability and error in L_A will result in much greater errors in the calculation of TL_w than will the estimate of T based on (3.13).

An accurate calculation of t may be made by determining L_r, as from Singh and Cracknell (1986), then finding L_a and solving for t_a using Durkee (1984). However, this more sophisticated calculation will not necessarily result in a significant improvement in the determination of L_w. The relationship between L_a and t_a depends on the type of aerosol and therefore may vary through the scene (Durkee et al., 1984; Durkee, 1984). Furthermore, without calculating the path radiance at every pixel, the error in assuming L_A or L_a constant will tend to exceed any absolute error associated with estimating T.

3.5. Sun Angle Correction and Reflectance

Interscene comparisons require a correction for sun angle to account for hourly and seasonal variations in the amount of incident irradiance, E_d. The calculation of reflectance provides a more general application by correcting not only for sun angle, but also for band width and placement, thereby permitting intercomparison of different spectral bands and different sensors. Reflectance also allows evaluation of the remotely sensed data in light of theoretical reflectance models.

The reflectance is determined using

$$R = QL_w/(E_o \cos \theta_o) \qquad (3.14)$$

where $Q = \pi$, and θ_o is the solar zenith angle.

We should note that irradiant reflectance models use the reflectance just below the water's surface (e.g. Gordon et al., 1975). This differs somewhat from R above the water surface

owing to refraction and reflection of the light by the surface, and changes in the radiance distribution (value of Q). The subsurface reflectance R_- can be expressed in terms of R

$$R_- = \frac{Q_- \, n^2}{Q \, (T_{s_-} T_{s_+})} \, R \qquad (3.15)$$

where T_s is the transmittance through the water surface from water into air (-) or air into water (+), n is the index of refraction for water, and Q_- is the relation between upwelling radiance and irradiance immediately below the surface. Austin (1974) calculated Q_-=5.1 at 480 nm. The index of refraction for brackish water is 1.335, with less than 1% variation for salinity or wavelength. T_{s-} and T_{s+} both equal 0.98. With $Q = \pi$, (3.15) leads to a relationship, $R_- = 3.0\ R$.

3.6. Determination of L and R

In this paper, reflectance will refer to the reflectance calculated using (3.14), with L_w found from (3.10) and (3.7) and T from (3.13). Underwater reflectance will refer to R_- of (3.15). From the digital count values (D_c), reflectance in band i can be determined using

$$R_i = f_{ri} D_{ci} - Z_{ri} \qquad (3.16)$$

where f_{ri} and Z_{ri} are given in Table 4. Radiance, L_i, is calculated from R_i using (3.4) with $Q = \pi$. The values in Table 4 are pre-launch calibrations with uncertainties of $\pm$5%.

The coefficients to determine L_* and E_o for the AVHRR are found in Table 4.

4. ESTUARINE REFLECTANCE AND SUSPENDED SOLIDS

4.1. General Principles of Ocean Color

Materials in the water change the reflectance of the water through their ability to absorb and scatter light. Several researchers have developed models from radiative transfer theory that show the relationships between reflectance, absorption, and scattering (Gordon et al., 1975; Jain and Miller, 1977; Philpot, 1981; Preisendorfer, 1976; Morel and Prieur, 1977). The Gordon et al. (1975) solution leads to an equation for subsurface irradiant reflectance at any wavelength:

$$R_-(\lambda) = \frac{.33\ b_b(\lambda)}{a(\lambda) + b_b(\lambda)} \qquad (4.1)$$

Table 4. Correction Coefficients for AVHRR

Satellite NOAA-	6	7	8	9	10
f_{r1}	.1071	.1068	.1060	.1063	.1059
Z_{r1}	4.144	3.440	4.162	3.846	3.528
E_{o1}[1]	155	156	157	157	157
f_{r2}	.1058	.1069	.1060	.1075	.1061
Z_{r2}	3.454	3.488	4.149	3.877	3.477
E_{o2}[1]	104	103	104	102	103

[1]Using Neckel and Labs (1984) E_{o1} becomes 1.05x greater, and E_{o2} 1.02x greater, than the values given above. At present, we prefer the above values for E_o.

where b_b is the backscatter coefficient and a is the absorption coefficient. Other models and simulations produce quite similar results indicating the validity of the form of (4.1).

The absorption and backscatter coefficients have units of inverse distance (i.e., m^{-1}). The absorption is the proportion of radiant energy lost per unit distance; b_b is the proportion of light scattered back into the hemisphere centered on the originating light beam. Jerlov (1976), Preisendorfer (1976), and other marine optics texts discuss details of a and b_b.

Both a and b_b can be expressed in terms of the absorption characteristics of the materials in the water:

$$a(\lambda) = a_w(\lambda) + a_d^*(\lambda)n_d + a_p^*(\lambda)n_p + a_s^*(\lambda)n_s \qquad (4.2a)$$

$$b_b(\lambda) = b_{bw}(\lambda) + b_{bs}^*(\lambda)n_s \qquad (4.2b)$$

where n denotes concentration, * denotes the specific absorption or backscattering coefficient, and subscripts w, d, p, and s denote, respectively, water, dissolved pigments, particulate organic pigments such as chlorophyll, and sediment and inorganic pigments.

In principle, if we knew a_w and b_{bw} and the specific coefficients for a and b_b, we could use values of R in three bands to calculate the concentrations of n_d, n_p, and n_s. In reality, only a_w and b_{bw} are known well (Smith and Baker, 1981). The chlorophyll-a component that dominates a_p^* is known fairly well (Prieur and Sathyendranath, 1981), but other pigments such as chlorophyll b and c, carotenoids, phycobilins, and phaeopigments, all of which can be optically significant in estuaries, may cause significant variations in a_p^*. For dissolved pigments the general variation of a_d^* with wavelength is known (Whitlock et al., 1982) but the suite and concentrations of the dissolved pigments that produce the absorption are quite variable. We know the range of values for the sediment absorption and backscatter (Bukata et al., 1981; Whitlock et al., 1981); however, a_s^* and b_{bs}^* will vary with grain size, and they may also vary with composition.

Some simplifying cases have allowed comparisons of R_- with n_p and n_s using different wavelengths (Morel and Prieur, 1977). Water absorbs strongly at longer wavelengths, and scatters strongly at shorter wavelengths (Figure 2). Chlorophyll and dissolved organic pigments (DOP) absorb strongly at blue and violet wavelengths (<500 nm) and chlorophyll-a also absorbs red light at 670 nm. For sediment, absorption depends on several factors. Iron oxide compounds absorb blue and violet light much like DOP. Scattering tends to be achromatic when a mixture of sizes is present, with a slight decrease with increasing wavelength (Van de Hulst, 1957).

The strong absorption by water at long wavelengths means that clear water will have negligible reflectance in red and near-IR light, i.e. $b_b << a$. This is generally true in oceanic waters. This red absorption together with the strong scattering of blue light by very clear oceanic waters results in the characteristic blue of the open ocean. As DOP is relatively low and constant in concentration in the ocean and the only particulates are plant cells, chlorophyll can easily be detected because it reduces the blue light reflectance, turning the water a turquoise or mint green. In terms of (4.1), clear water has $b_b > a$ for blue light, whereas chlorophyll-bearing water has $a > b_b$. Chlorophyll has a minimal effect on the green light reflectance (Austin, 1974), therefore a ratio of reflectance of blue light to green light can show the chlorophyll concentration. This behavior is the basis for the CZCS chlorophyll algorithm (Gordon et al. 1983).

In estuaries and near-coastal water, the situation is much different. DOP and sediments with their iron content occur in much higher and more variable concentrations. Therefore a blue/green reflectance ratio is ineffective for measuring chlorophyll. The comparatively high and variable DOP and chlorophyll content and the potential iron component reduce the reflectance at shorter wavelengths, producing a maximum

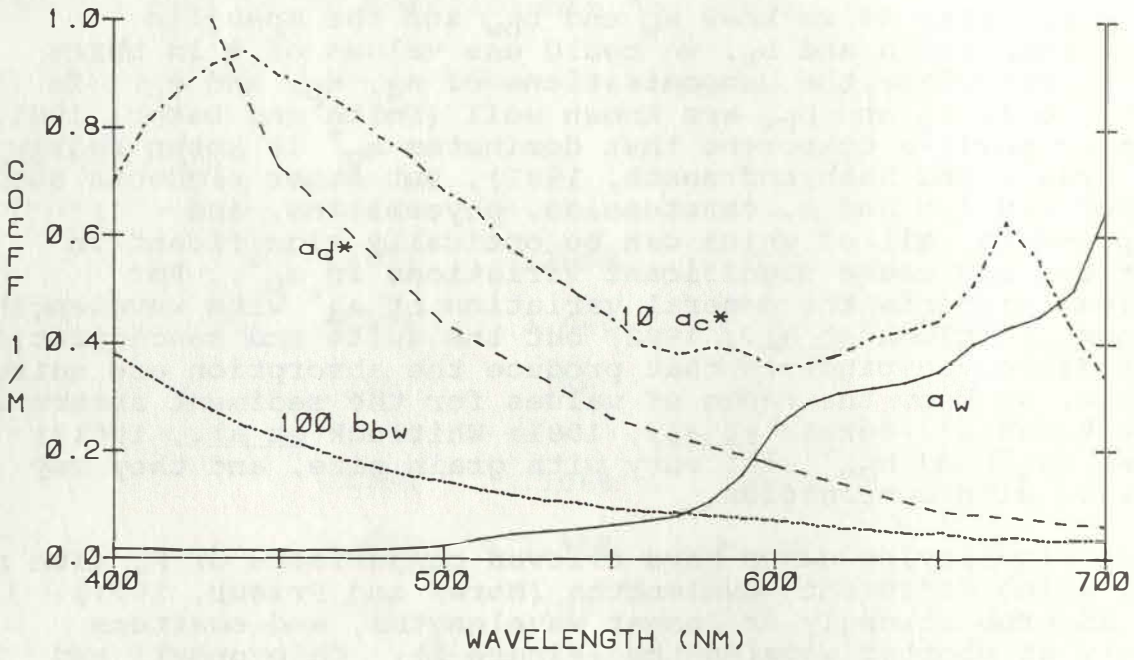

Figure 2: Absorption and backscatter coefficients for water (a_w, b_{bw} from Smith and Baker, 1981), chlorophyll (a_c' from Prieur and Sathyendranath, 1981) and dissolved pigments (a_d' from Witte et al., 1982).

reflectance between 550-650 nm (yellow or orange light). In cases of extremely high sediment loads (>200 mg/l) the maximum reflectance maybe in the red (650-700 nm and near-IR (>700 nm) wavelengths. Hence sediment laden coastal waters have a milky brown appearance.

4.2. Generalized Reflectance Relationships for Suspended Solids in Turbid Water.

The reflectance of estuarine waters is usually dominated by the sediment content. Accordingly, any model to interpret remotely sensed reflectance must treat for the effects of sediment concentration.

Empirical calculations have shown a generalized relationship between R and n_s as

$$R = m \log (n_s) + b \qquad (4.3)$$

where m and b are constants of regression (Stumpf, 1987). The logarithmic relationship also applies to L^* and L_w (Klemas et

al., 1974; Munday and Alfoldi, 1979) because they are linearly related to R (cf. (3.8) and (3.12).

Although sediment dominates reflectance, other factors, such as pigment content and sediment size, should enter into the relationship with reflectance. These are not accounted for in (4.3). A physical relationship could incorporate these effects in such a way to allow for adjustment of the coefficients with changes in the materials in the water. It may also explain the logarithmic relationship.

To incorporate other effects on the relationship between R and n_s, we can use a modification of (4.1). In turbid water, all backscatter can be considered to result from sediment, i.e. $b_b = b_{bs}$. The absorption can be separated into absorption due to sediment and absorption due to pigments and water. Then (4.1) can be rewritten as

$$R(\lambda) = \frac{0.33\ b_{bs}^*(\lambda)}{S^*(\lambda) + a_x(\lambda)/n_s} \qquad (4.4)$$

where $S^* = a_s^* + b_{bs}^*$ accounts for sediment, and $a_x = a_w + a_d^* n_d + a_p^* n_p$ includes water and organic pigments. Equation (4.4) may be called the turbid water approximation. In this form, we find that R=0 when n_s=0, which mathematically allows for the clearwater atmospheric correction. (For blue and green light in clear oceanic water, this approximation is not appropriate because R≠0 when n_s=0.) In general, a_x is greater than 1 m^{-1} for red and near-IR light, and S^* is between 0.01 and 0.1 m^{-1} (Bukata et al., 1981; Whitlock et al. 1981). Therefore, for n_s=1 ($\log_{10} n_s$ =0)--the minimum value appropriate for the turbid water model--we find $R \simeq b_{bs}^*/a_x$; and for n_s large, (4.4) has the asymptote $R = b_{bs}^*/S^*$.

Munday and Alfoldi (1979) modified (4.1) and showed a similar relationship to that in (4.4) by comparing $1/L^*$ (as a surrogate for 1/R) with $1/n_s$. They obtained correlation coefficients of >0.85 both for L^* vs log n_s and for $1/L^*$ vs. $1/n_s$ with n_s varying between 2 and 200 mg/l.

In constrast to (4.3) or other statistical relationships, (4.4) provides for greater flexibility in equating reflectance and sediment concentration. Simple curve fitting of (4.4) to data sets of R and n_s will permit estimation of sediment concentration. However, by including backscatter and absorption coefficients, the relationship allows adjustment of the calibration coefficients for changes in grain size (affecting b_{bs}^* and S^*) and pigment concentration (affecting a_x^*, as described in chapter 5).

4.3. Reflectance Variations with Grain Size and Absorption.

Because a_x is about an order of magnitude larger than S^*, R, while varying primarily with n_s, will also depend on b_b^* and a_x (Figure 3). In turn, b_b^* depends directly on particle characteristics. The relation between b_{bs} and particle cross-sectional area is

$$b_{bs}^* n_s = b_Q \, (\pi/4) \, d^2 \, N \qquad (4.5)$$

where b_Q is the backscattering efficiency (dimensionless), d is the effective particle diameter, and N is the concentration in # of particles per volume. If we take the particles to be spherical, then

$$n_s = (\pi/6) \rho d^3 \, N \qquad (4.6)$$

where is the particle density. Combining these we obtain

$$b_{bs}^* = (3/2) \, b_Q/(\rho d) \qquad (4.7)$$

Therefore, there is an inverse relationship between b_{bs}^* and (ρd):

$$b_{bs}^* \propto 1/(\rho d) \qquad (4.8)$$

S^* will also vary in the same fashion with (d).

The optical diameter, d_o, will be expressed as

$$d_o = (\rho d)/\rho_w \qquad (4.9)$$

where ρ_w is the water density.

If we define

$$b_{bs}^* = b_{bs}^{*\prime}/(\rho_w d_o) \qquad (4.10)$$

where $b_{bs}^{*\prime}$ is the backscatter coefficient for a reference diameter (similarly for S^*), (3.4) becomes (dropping λ)

$$R = \frac{0.33 \, b_{bs}^{*\prime}/(\rho_w d_o)}{S^{*\prime}/(\rho_w d_o) + a_x/n_s} \qquad (4.11)$$

For n_s of low to moderate values, R will tend to vary with the inverse of d_o. As the grain size increases (b_{bs}^* and S^* decreasing) in curves 1-3 of Figure 3b, the reflectance decreases for a given concentration. Note that as n_s becomes large (say > 200 mg/l) differences due to grain size tend to disappear if b_{bs}^*/S^* is constant. However, the asymptote at b_{bs}^*/S^* is apparent by the difference between curve 4 and curves 1-3.

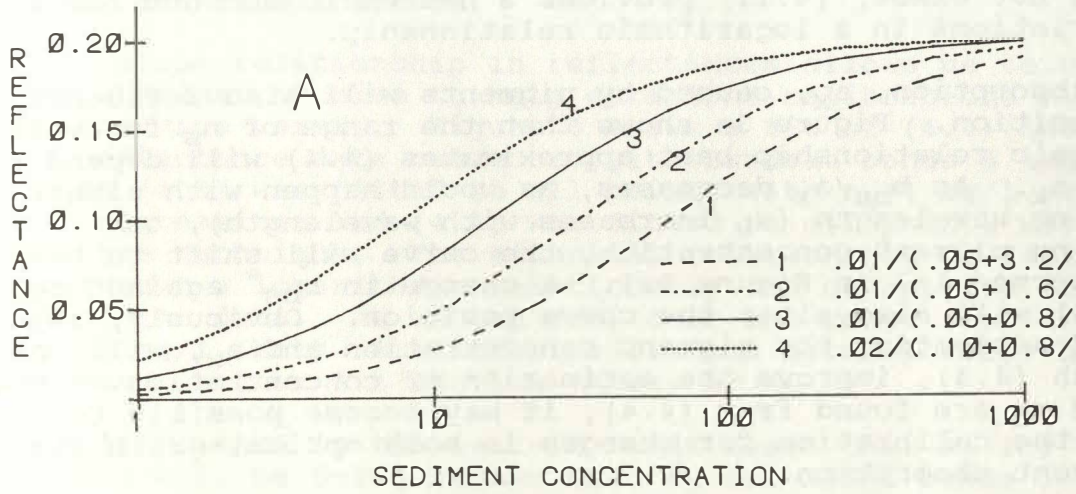

Figure 3a: Variation in R vs. n_s from (4.4). Changes in a_x for constant b_{bs}* and S* (curves 1-3); curve 4 shows a change in b_{bs}* and S* for comparison. Increasing a_x descreases the reflectance at a given concentration.

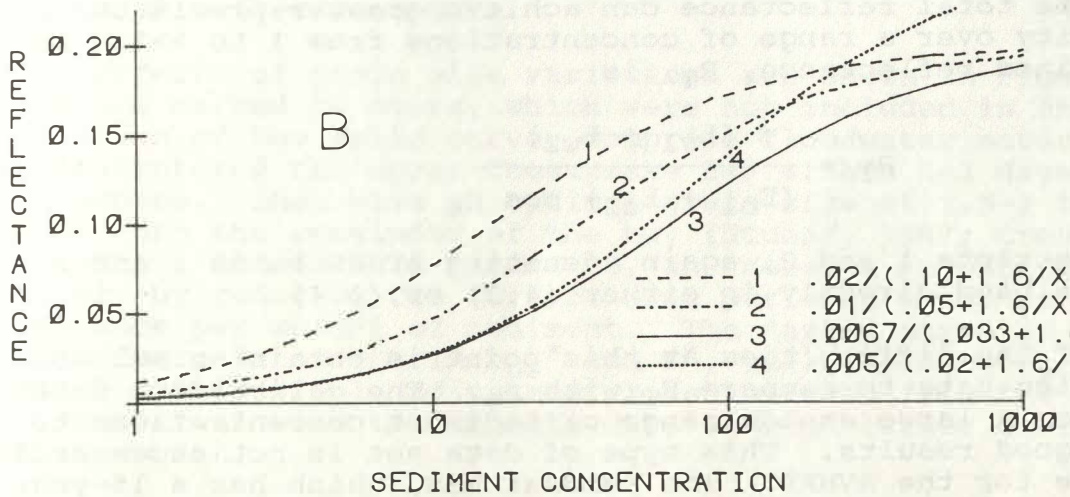

Figure 3b. Changes in optical grain size, with b_{bs}*/S* constant (=0.6) for curves 1-3. Increasing grain size (decreasing b_{bs}* and S*) produces a decrease in reflectance. Curve 4, with b_{bs}*/S*=0.75 shows the change in the high asymptote with change in sediment optical characteristics.

Given the change in slope caused by b_{bs}^*, we could write (4.3) as

$$R = (M/d_o) \log (n_s) + B \qquad (4.12)$$

Although not exact, (4.12) provides a heurestic account for grain size variations in a logarithmic relationship.

The absorption, a_x, caused by pigments will also influence curve position. Figure 3a shows that the range of n_s for which a logarithmic relationship best approximates (4.4) will depend on b_{bs} and a_x. As b_{bs}/a_x decreases, as would happen with either increasing wavelength (a_w increases with wavelength), or increasing pigment concentration, the curve will shift to the right (curves 1-3 in Figure 3a). A change in b_{bs}^* against a_x (curve 4) will also alter the curve position. Obviously, any means of estimating the pigment concentration and a_x, will when used with (4.4), improve the estimation of concentration. Once b_{bs}^* and a_x are found from (4.4), it may become possible to correct the calibration for changes in both optical grain size and pigment absorption.

4.4. Calibration in Turbid Water

The relationships of (4.3) and (4.4) between n_s and R would avoid interference from pigments if only the near-IR band is used. However, in clear to moderately turbid water, the strong absorption by water produces only slight to moderate changes in the near-IR reflectance. Combining the red and near-IR bands to obtain the total reflectance can achieve greater precision and sensitivity over a range of concentrations from 1 to >>100 mg/l. The combined reflectance, R_T, is

$$R_T = \frac{\pi (L_{w1} + L_{w2})}{(E_{o1} + E_{o2}) \cos \theta_o} \qquad (4.13)$$

With subscripts 1 and 2, again, denoting AVHRR bands 1 and 2. R_T can be used directly in either (4.3) or (4.4).

One of the difficulties at this point is obtaining suitable calibration data to compare R_T with n_s. The calibration data must cover a large enough range of sediment concentrations to provide good results. This type of data set is not necessarily available for the AVHRR. The Landsat MSS, which has a 15-year archive, could be drawn on for calibration.

The similarity in the spectral bands between Landsat MSS bands 5 and 6 (bands 1 and 2 on Lansat 4 and 5) and AVHRR bands 1 and 2 (Table 2) can allow comparison of the two data sources for calibration. Figure 4 shows the relationship between the bands for Landsat MSS and AVHRR reflectances for scenes taken 80

minutes apart in the lower Chesapeake Bay. The AVHRR band 1 has effectively the same reflectance response as MSS band 5. AVHRR band 2 differs by 20% from MSS 6, which should be a consistent deviation, given that the AVHRR band extends further into the strongly absorbed infrared.

This close relationship in reflectances allows us to use the 15 year Landsat archive to help establish calibrations for the AVHRR (or vice versa). Figure 5 shows a fit of (4.3) and (4.4), using reflectance data collected with Landsat bands 5 and 6. Equation (4.3) was fitted to all points with n_s>4 mg/l using linear regression; and (4.4) was fitted to all points with an interative technique. The sigmoidal relationship of (4.4) assures that a logarithmic relationship can be applied to some range of the data. As we can see, over the range from 7 to at least 70 mg/l, both relationships fit the data closely; however, (4.4) has a better fit for low values of n_s.

The difference in the near-IR bands means that R_T for MSS bands 5+6 will be 5-10% higher than R_T for AVHRR bands 1+2 for a given n_s. The data for Landsat in Figure 5 covers a greater range of concentrations than that currently corresponding to AVHRR data in Chesapeake or Delaware Bay. The current calibrations for the AVHRR (Table 5) are calculated from this data set.

Sample data collected in Chesapeake Bay by the University of Delaware (provided by J. Pennock, pers. comm.) appears in Figure 6, showing the fit of this calibration to an independent data set using AVHRR reflectance data.

The effects of grain size variations are shown in Figure 5. The values marked by stars, which were not included in the calculation of the solid curve, comprise floodwater materials that had entered the upper Chesapeake Bay within 1-2 days of the the overpass. They have an optical grain size of 1.5-2 times greater than the remainder of the bay (Stumpf, 1987; Cronin <u>et al.,</u> 1981). As shown in Figure 3B, an increase in optical diameter, by reducing the surface area per unit mass, reduces the reflectance per weight of sediment. The dashed curve in Figure 5 shows a decrease of 50% in b_{bs}^* and S^*, while holding a_x constant. This simple adjustment fits the data from the upper Bay, consistent with the <u>in situ</u> data showing larger grain size in that region.

In Figure 6, for n_s=22 mg/l, the sample was taken in the turbidity maximum, an area characteristically having larger grain sizes. The deviation of this data point from the curve, although not verified as resulting from a difference in grain size, is consistent with a larger optical diameter.

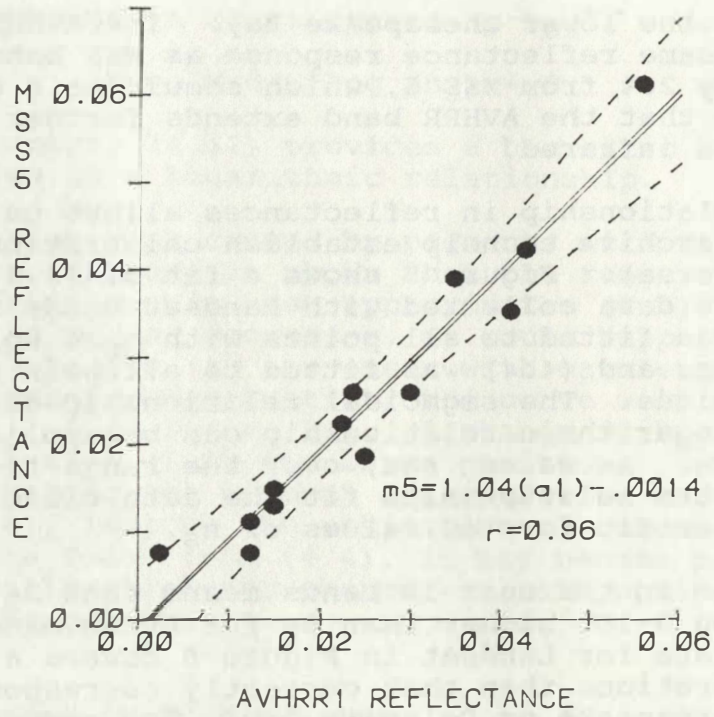

(A)

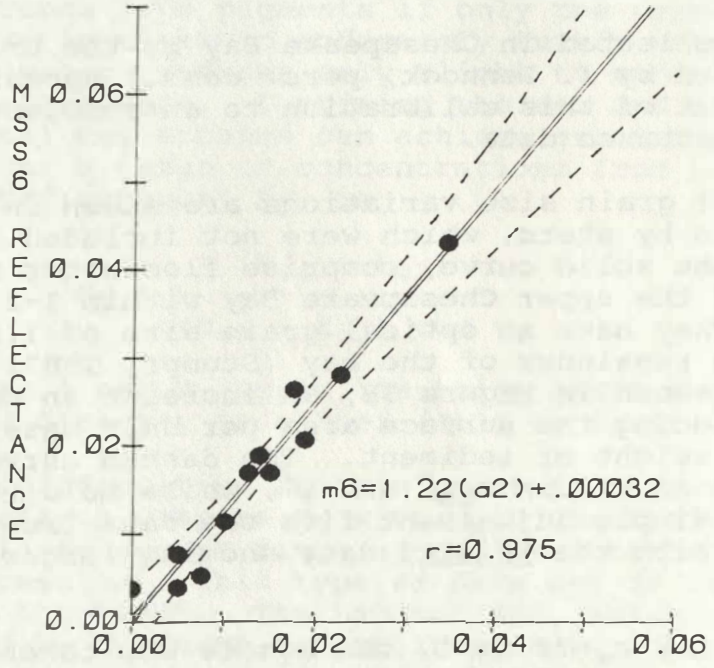

(B)

Figure 4: AVHRR and MSS reflectances in lower Chesapeake Bay; MSS taken at 1000EST, AVHRR at 0840 EST.

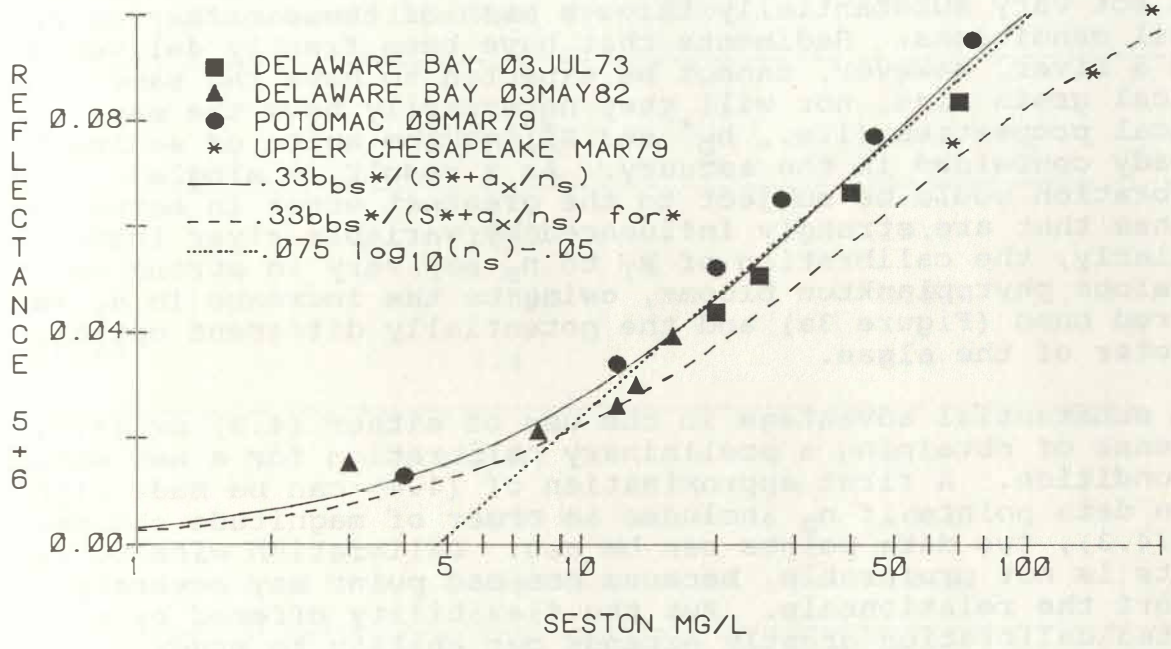

Figure 5: Reflectance vs. sediment concentration using (4.1) and (4.4), and data from Klemas et al., (1974) and Stumpf (1987).

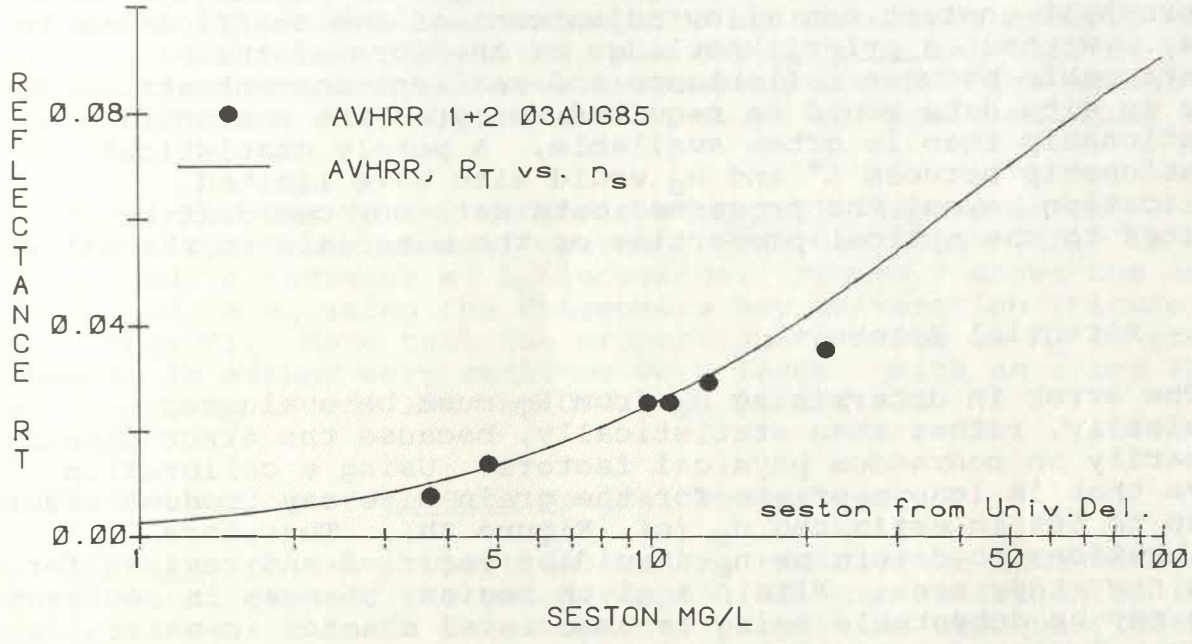

Figure 6: R_T from AVHRR vs. n_s collected in Chesapeake Bay (data from Univ. Delaware, Church and Pennock).

The very close fit (R_T within 10% for a given n_s) between the different data sets in Figure 5 suggests that optical grain size does not vary substantially through much of these estuaries under normal conditions. Sediments that have been freshly delivered from a river, however, cannot be expected to have the same optical grain size, nor will they necessarily have the same optical properties (i.e., b_b^* and S^*) as the suite of sediments already contained in the estuary. As a result, a single calibration would be subject to the greatest error in estuarine reaches that are strongly influenced by variable river loads. Similarly, the calibration of R_T to n_s may vary in strong and anomalous phytoplankton blooms, owing to the increase in a_x in the red band (Figure 3a) and the potentially different optical diameter of the algae.

A substantial advantage in the use of either (4.3) or (4.4) is the ease of obtaining a preliminary calibration for a new estuary or condition. A first approximation of (4.4) can be made with three data points if n_s includes an order of magnitude change; for (4.3), two data points can be use. Calibration with so few points is not preferable, because one bad point may severely distort the relationship. But the flexibility offered by a limited calibration greatly expands our ability to study different areas and environmental conditions.

The calibration, once chosen, can be routinely verified using only a modest field effort. Variations in the coefficients could be compared and interpreted with real changes in the estuarine materials. Similarly, knowledge of changes in particle size or chlorophyll content can allow adjustment of the coefficients in (4.4). Without a priori knowledge of the form of the relationship between reflectance and sediment concentration, far more in situ data would be required to establish a significant relationship than is often available. A purely statistical relationship between L^* and n_s would also have limited application beyond the processed data set, nor could it be related to the optical properties of the materials in the water.

4.5. Potential Errors

The error in determining n_s from R_T must be evaluated physically, rather than statistically, because the error depends primarily on nonrandom physical factors. Using a calibration curve that is inappropriate for the grain size may produce errors of up to 50% in estimated n_s (cf. Figure 3b). Therefore, calibrations to determine n_s should be verified and revised for each new study area. Within a given region, changes in sediment type may be detectable owing to associated changes in water color. Areas of potential variations in the calibration may then be identifiable using the techniques described in chapter 5.

Table 5. Calibrations to determine n_s from R_T using (4.3) or (4.4) for the data sets shown in Figure 5. R_T was found using (4.13). All regressions had $r^2 > 0.9$.

	AVHRR 1+2	MSS 5+6
1/m	17.0	15.3
b/m	0.535	0.534
$10^{(b/m)}$	3.4	4.4
a_x	3.1	2.0
b_{bs}*	.027	.021
S*	.065	.048

Equation (4.3) is simple to use in a calibration with linear regression of R vs. log n_s. However, unlike (4.4), the accuracy of (4.3) will be limited to about one order of magnitude variation in n_s (cf. Figures 3 and 5). Extrapolation to determine n_s outside that range will be subject to error. For R low, n_s will be overestimated, and for R large, n_s will be underestimated with the error increasing with R. The actual amount of error will depend on the slope and positioning of the curves.

The error due to the estimate of L_A will depend on the variability of the aerosol content. The variation (dL_A) in L_A will tend to increase as L_A increases. Figure 7 shows the error in R_T and in n_s using the Chesapeake Bay calibration (Figure 5 and Table 5). Note that the proportionate error in n_s is greater when R_T is either very small or very large. With an error in R of 0.005, n_s is off 15%; at 0.01, n_s is off 33%.

4.6. Detection of <u>In Situ</u> Optical Properties.

<u>In situ</u> optical properties such as the diffuse attenuation coefficient (k) and the Secchi depth (SD) can be estimated from reflectance. Because these optical properties also vary with the grain size of the sediments, they may be estimated with greater accuracy than possible for n_s.

Using the same notation as before, the diffuse attenuation coefficient can be expressed as (Smith and Baker, 1978)

$$k = k_w + k_p{}^* n_p + k_d{}^* n_d + k_s{}^* n_s \qquad (4.14)$$

In turbid water, we can make a reasonable assumption that $k = k_s{}^* n_s$. Also $k \propto a + b_b$ (Gordon et al., 1975), so $k_s{}^*$ varies inversely with the optical diameter. If we substitute $k/k_s{}^{*\prime}$ for n_s in (4.11) we obtain

$$R = \frac{.33\ b_{bs}{}^{*\prime}/d_o}{S^{*\prime}/d_o + a_x\ k_s{}^{*\prime}/[kd_o]} \qquad (4.15)$$

Hence, when comparing R and k in turbid water, the grain size effect will drop out, leaving

$$R = \frac{.33\ b_{bs}{}^{*\prime}}{S^{*\prime} + a_x\ k_s{}^{*\prime}/k} \qquad (4.16)$$

Similarly, the Secchi depth also varies with the optical diameter (Postma, 1961):

$$SD \propto \rho_w d_o/n_s \qquad (4.17)$$

If absorption by pigments is significant, the relationship between reflectance and either k or SD may change considerably. As attenuation caused by absorption increases, the reflectance decreases. Identification of changes in pigment absorption would then be an advantage in determining the true value of k or SD.

Using (4.14) or (4.17), we can substitute into (4.3) or (4.4) (the latter producing eq. 4.15) to determine a calibration between R and k or SD. As the wavelength of maximum light penetration in estuarine waters is about 600 nm, within the spectral range for AVHRR band 1, R_1 may be more suitable than R_T for determining k for white light.

In situ data at present is limited, so we can produce only a tentative relationship for a narrow range of SD (Figure 8). Inclusion of additional and concurrent satellite and in situ data will better substantiate the relationship. We should note that estimating turbidity from satellite may be more accurate than measuring it with a Secchi disk. Secchi depth measurements can vary greatly, depending on the operator and they will vary with cloud cover and sun angle. These problems are avoided when using satellite, because the same sensor is used, the measurements can only be taken with full sunlight, and a sun angle correction is readily made (which rarely happens for in situ Secchi depth measurements).

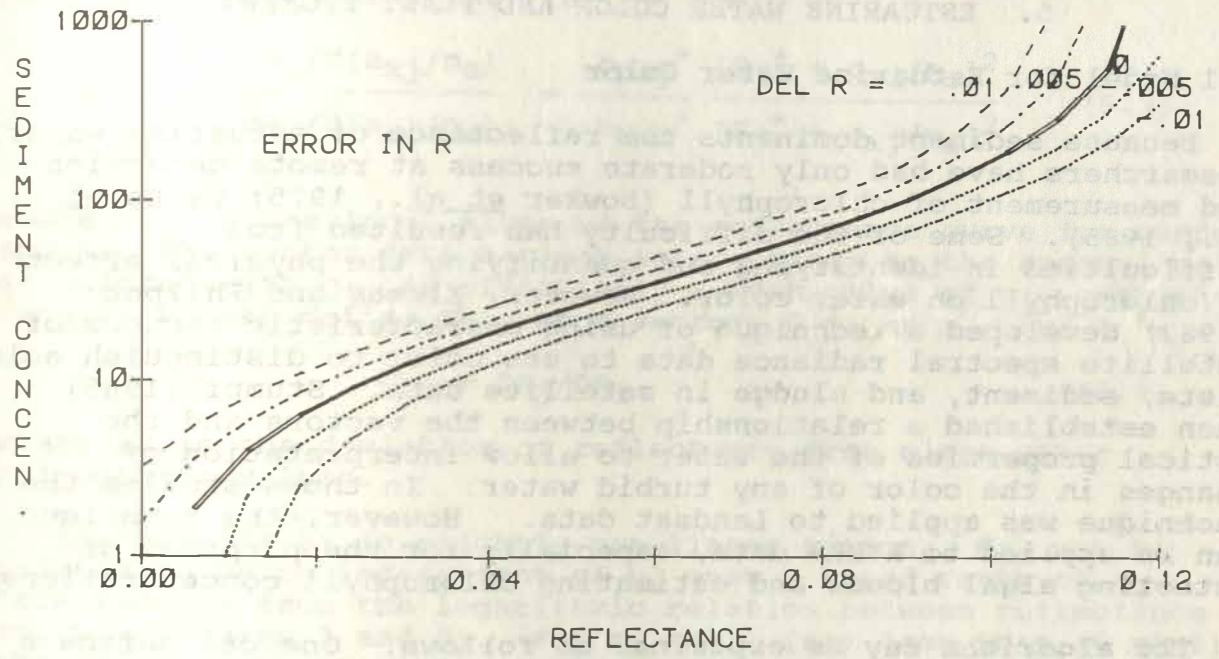

Figure 7: Error in calculated sediment concentration caused by atmospheric correction error (del R).

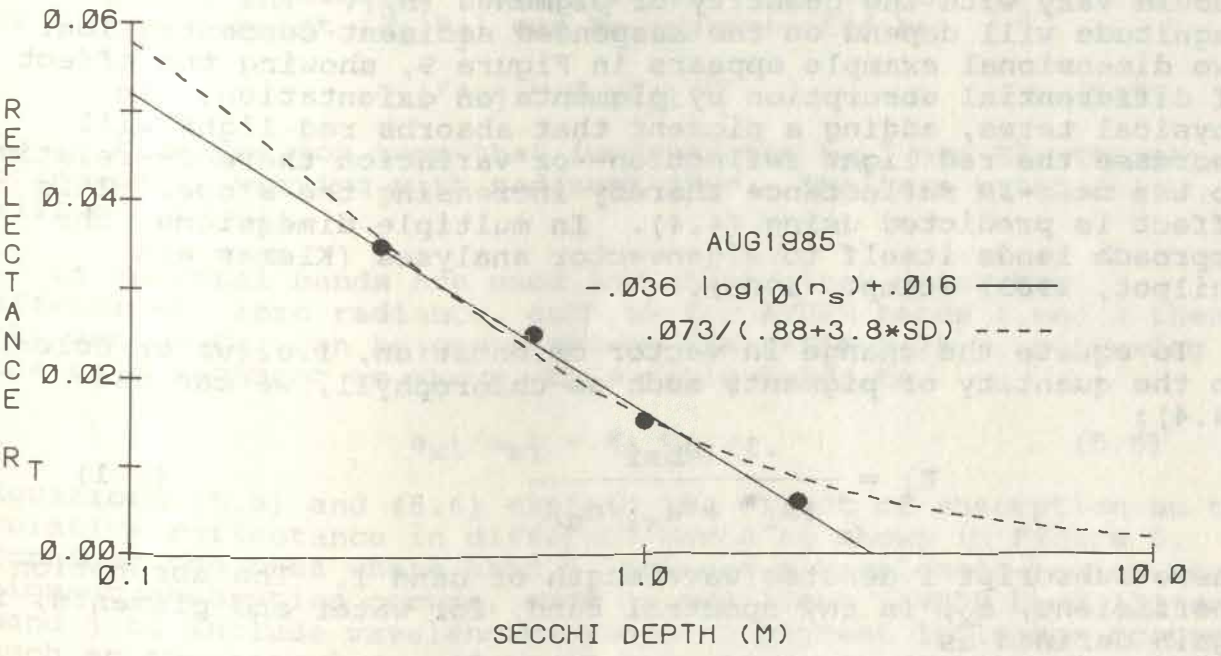

Figure 8. Reflectance vs. Secchi Depth for data collected 02-06 August 1985. Because of the limited data set, additional data will be needed to validate the displayed relationships.

5. ESTUARINE WATER COLOR AND PLANT PIGMENTS

5.1 Model for Estuarine Water Color

Because sediment dominants the reflectance of estuarine water, researchers have had only moderate success at remote detection and measurement of chlorophyll (Bowker et al., 1975; Catts et al., 1985). Some of the difficulty has resulted from difficulties in identifying and quantifying the physical effect of chlorophyll on water color. However, Klemas and Philpot (1983) developed a technique of using characteristic vectors of satellite spectral radiance data to use color to distinguish acid waste, sediment, and sludge in satellite data. Stumpf (1985) then established a relationship between the vectors and the optical properties of the water to allow interpretation of changes in the color of any turbid water. In those studies the technique was applied to Landsat data. However, the technique can be applied to AVHRR data, especially for the purposes of detecting algal blooms and estimating chlorophyll concentrations.

The algorithm may be explained as follows. One can define a coordinate system, or "color" space, using the radiance in the bands as the axes. A vector may extend from an origin that is defined by clearwater radiance to a coordinate determined by each data point in the scene. Because pigment and water absorption characteristics vary with wavelength, the vector orientation should vary with the quantity of pigments (n_p). The vector magnitude will depend on the suspended sediment concentration. A two dimensional example appears in Figure 9, showing the effect of differential absorption by pigments on orientation. In physical terms, adding a pigment that absorbs red light will decrease the red light reflection--or variation thereof--relative to the near-IR reflectance thereby increasing the slope. This effect is predicted using (4.4). In multiple dimensions, the approach lends itself to eigenvector analyses (Klemas and Philpot, 1983; Stumpf, 1985).

To equate the change in vector orientation, i.e. water color, to the quantity of pigments such as chlorophyll, we can use (4.4):

$$R_i = \frac{.33\ b_{bsi}^*}{(S_i^* + a_{xi}/n_s)} \qquad (5.1)$$

where subscript i denotes wavelength of band i. The absorption coefficient, a_x, in any spectral band, for water and pigments, is again defined as

$$a_x = a_w + a_d^* n_d + a_c^* n_c. \qquad (5.2)$$

The reflectance in any band varies with (a_x/n_s). Therefore, the relative change in reflectance in bands i and j at any

particular spectral point, is

$$c_{ji} = \frac{dR_j/d(a_{xj}/n_s)}{dR_i/d(a_{xi}/n_s)} = \frac{b_{bsj}^*}{b_{bsi}^*} \frac{[S_i^* + a_{xi}/n_s]^2}{[S_j^* + a_{xj}/n_s]^2} \qquad (5.3)$$

where c_{ji} is the local slope of the reflectance curve for bands i and j. The vector from a clear water origin to the spectal point associated with c_{ji} is effectively a mean value of c_{ji} over that range. We can define this mean vector, C_{ji}, as

$$C_{ji} = DR_j/DR_i \qquad (5.4)$$

where DR is the deviation of reflectance from clear water reflectance values.

Although (5.3) is slightly non-linear with n_s, C_{ji} can be treated as being independent of n_s over a broad range of n_s. This results from the logarithmic relation between reflectance and n_s (Figures 3 and 5). For n_s small (say less than 10 mg/l), the terms in brackets in (5.3) approach $(a_{xi}/a_{xj})^2$. As n_s becomes large, they approach $(S_i^*/S_j^*)^2$; however R varies with $\log(n_s)$ (chapter 3), meaning that large values of n_s have exponentially less influence on C_{ji} than do small values. Hence, the a_x absorption will control vector orientation for low to moderate reflectances. Therefore the mean vector (C_{ji}) from the origin to a point (R_i,R_j) can be approximated by

$$a_{xi}/a_{xj} = G_s \, C_{ji}^{.5} \qquad (5.5)$$

G_s is a correction term that incorporates b_{bs}^* and S^*, thereby principally varying with sediment type. The term water color will denote C_{ji}.

If spectral bands are used for which clear water has effectively zero radiance, such as for AVHRR bands 1 and 2 then the vector C_{ji} can be expressed by the ratio R_j/R_i. Following the same argument as above, this ratio leads to

$$a_{xi}/a_{xj} = G_s \, C_{ji} \qquad (5.6)$$

Equations (5.5) and (5.6) explain the effect of absorption on the relative reflectance in different bands as shown in Figure 9. Consider the case where band i includes a wavelength region where pigment absorption occurs, such as red light (AVHRR band 1), and band j to include wavelengths where no pigment influence occurs, such as the near-infrared (band 2). Hence, variations in pigment concentration would affect the reflectance in red band i, but not in near-IR band j. An increase in pigment concentration (n_p) would reduce R_i, causing the shift seen in Figure 9. The ratio, C_{ji}, normalizes for the reflectance change caused by sediment.

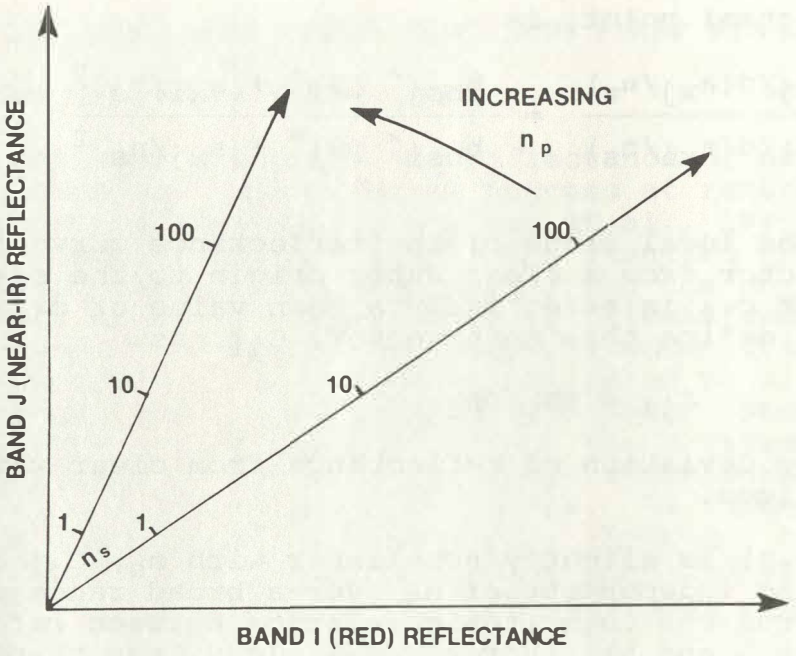

Figure 9: Effects of pigments (n_p) and suspended solids (n_s) on radiance vectors in 2-dimensions. An increase in absorption by pigments in band 2 reduces the change in band 2 reflectance relative to band 1.

Namely, for a given sediment concentration, the reflectance of red light will decrease when the pigment concentration increases, whereas reflectance of near-infrared light will remain relatively unchanged, hence DR_j/DR_i (and so C_{ji}) will increase (Figure 9 and (5.6)). Similarly, at high pigment concentrations, pigment absorption will reduce reflectance changes in a red band i; therefore, R_i will vary less rapidly than R_j (i.e. C_{ji} higher) as n_s changes, than it will at lower pigment concentrations.

Catts et al. (1985) used this type of red/infrared response as part of an algorithm that compared simulated Landsat data to the chlorophyll content in San Francisco. The concept is also analogous to that used in the Gordon et al. (1983) algorithm for the CZCS using blue and green bands.

Knowing the absorption coefficients, we could, in principle, use (5.2) and (5.5) or (5.6) to estimate the absolute quantity of pigment. In practice, when the dissolved component n_d does not vary or a_d^* is very small (as for red light), then $a_x=a_c^*n_c$. We can then relate the chlorophyll concentration to water color through

$$n_c = h\, C_{ji}^{.5} + p \qquad (5.7)$$

or

$$n_c = H\, C_{ji} + P$$

where h, p, H, and P are constants and n_c is the chlorophyll concentration. Linear regression could be used to establish parameters that directly equate C_{ji} with n_c.

Because (5.3) does contain a non-linearity, which will make C_{ji} partially dependent on n_s, comparisons of C_{ji} are best made between areas having comparable R (or radiance) or n_s; preferably R should differ less than a factor of 4 for comparison (Stumpf, 1985). Also, variations in the sediment spectral response of b_{bs}^* and S^* may alter G_s and so change the relationship in (5.7).

5.2. Calibration for AHVRR

The AVHRR bands will indicate the presence of chlorophyll-a, but being fairly broad will also respond to other pigments. Band 1 will have a slight sensitivity to the other chlorophylls and to other pigments such as phycocyanin. This broad response poses no problem for determining relative variations of pigment quantity in a given scene or in determining differences when chlorophyll-a concentrations are high. Yet, when chlorophyll-a concentrations are low, response from other pigments may obscure the association of C_{ji} with chlorophyll-a, precluding reliable estimates of low concentrations of the pigment. This problem is less severe for red light than for blue light, which more pigments absorb.

Figure 10 shows variation of chlorophyll-a concentration with C_{ji} for AVHRR bands 1 (=i) and 2 (=j). As expected, the regression lines for (5.5) and (5.6) nearly overlie. In turbid water n_s varies 2-3 power whereas a_x varies 2-3 fold, therefore C_{ji} may be more sensitive to small fluctuations in the optical properties. Also, several pigments will effect C_{ji} when used with the AVHRR, for example, phaeophytin, which has the same red light absorption as chlorophyll-a, and chlorophyll-b and -c. Therefore calibration for chlorophyll-a or chlorophyll-a + phaeophytin will require more data than for determination of n_s from R_T.

Data only for 14 April 1982, which had ship and satellite data taken within a few hours (from Tyler and Stumpf, 1987) appear in Figure 11. The plot shows that C_{ji} can give good discrimination for n_c > 10 µg/l. For lower chlorophyll concentrations, comparison of <u>in situ</u> and satellite distributions indicates that C_{ji} can discriminate regions having n_c of 5-10 µg/l from those having <5 µg/l.

Many algorithms attempting to quantify chlorophyll concentrations have used sediment induced reflectance as a surrogate, which limits their applicability. Therefore, distinguishing reflectance from water color becomes an important component of this algorithm. Figures 12a and 12b display R_T and C_{ji}, respectively, for the 14 April 1982 NOAA-7 AVHRR image of Chesapeake Bay. In Figure 12a, clouds and haze (masked in white) cover the lower bay and continue offshore. Clearer water is evident in the Bay axis, with more turbid water in the tributary estuaries, and the highest reflectance (R_T>0.09) at the turbidity maximum in the upper Bay. Figure 12b shows low values of C_{ji} at and above 39°N (Annapolis), the region of the turbidity maximum (Figure 12a), and moderate to low C_{ji} west of 77°W (Morgantown) in the Potomac. The satellite data also indicate moderate values in the lower Potomac and lower Chesapeake Bay. Very high values of C_{ji}, indicative of a bloom, appear in the Potomac River about 77°W. The distribution of chlorophyll predicted from C_{ji} corresponds exactly to that found from ship on the same day (Tyler and Stumpf, 1987). The reflectance shows no variation across the bloom. Other areas having the same reflectance have much different values for C_{ji}.

The slight non-linearity in (5.3) will tend to cause C_{ji} to increase with R_T. This effect is not evident for R_T up to 0.10 (a common range in these estuaries). The ability to clearly discriminate between pigment concentration and turbidity is a significant strength of this method.

5.3 Errors and Limitations

The predominant error in C_{ji} results from the uniform atmospheric correction. This correction can result in two forms of error: 1) a scene bias produced by an incorrect estimate of the atmosphere in either band, and 2) a local error cause by inhomogeneities in the atmosphere. The error, e, in the observed C_{ji}' is

$$\frac{E_{oj}}{E_{oi}}(C_{ji}-C_{ji}') = e = \frac{(L_{wj}'/L_{wi}')(dL_{Ai}/L_{wi}') - (dL_{Aj}/L_{wi}')}{(1 - dL_{Ai}/L_{wi}')} \qquad (5.6)$$

where C_{ji} is the real value; $C_{ji}' = (L_{wj}'/L_{wi}')(E_{oi}/E_{oj})$ is the measured value; L_w is the upwelled radiance from the water reaching the satellite; dL_A is the difference between real and assumed atmosphere ($=L_w-L_w'$). When e is positive C_{ji}' is an underestimate of the true C_{ji}. The clearwater subtraction, by using the darkest clearwater, will tend to underestimate the real atmosphere (dL_A>0).

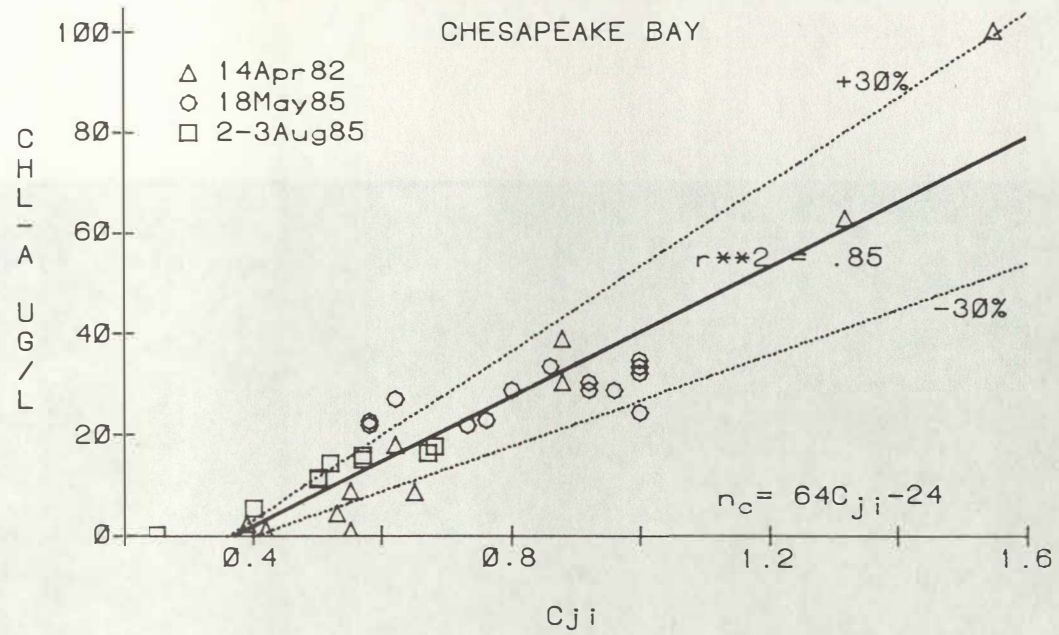

Figure 10: C_{ji} and chlorophyll-a data for Chesapeake Bay, 14 April 82 data from Tyler and Stumpf (1987); May 85 chlorophyll data collected 17 May by Tuttle and Malone, Univ. Maryland; Aug 85 data collected 05-06 Aug by U.S. EPA monitoring program.

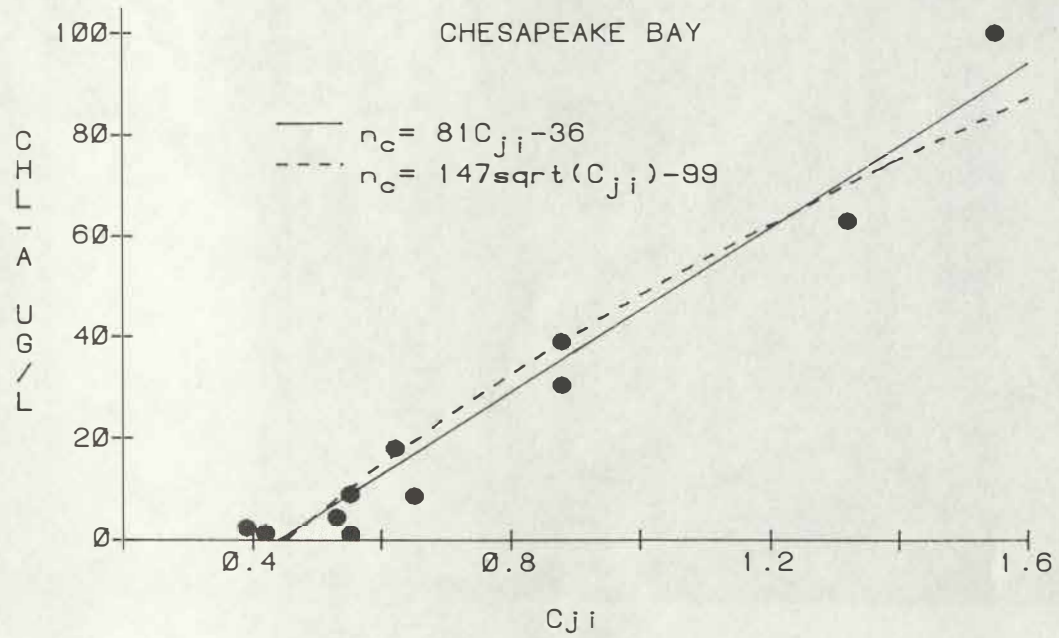

Figure 11: C_{ji} vs. chlorophyll-a for 14 April 1982.

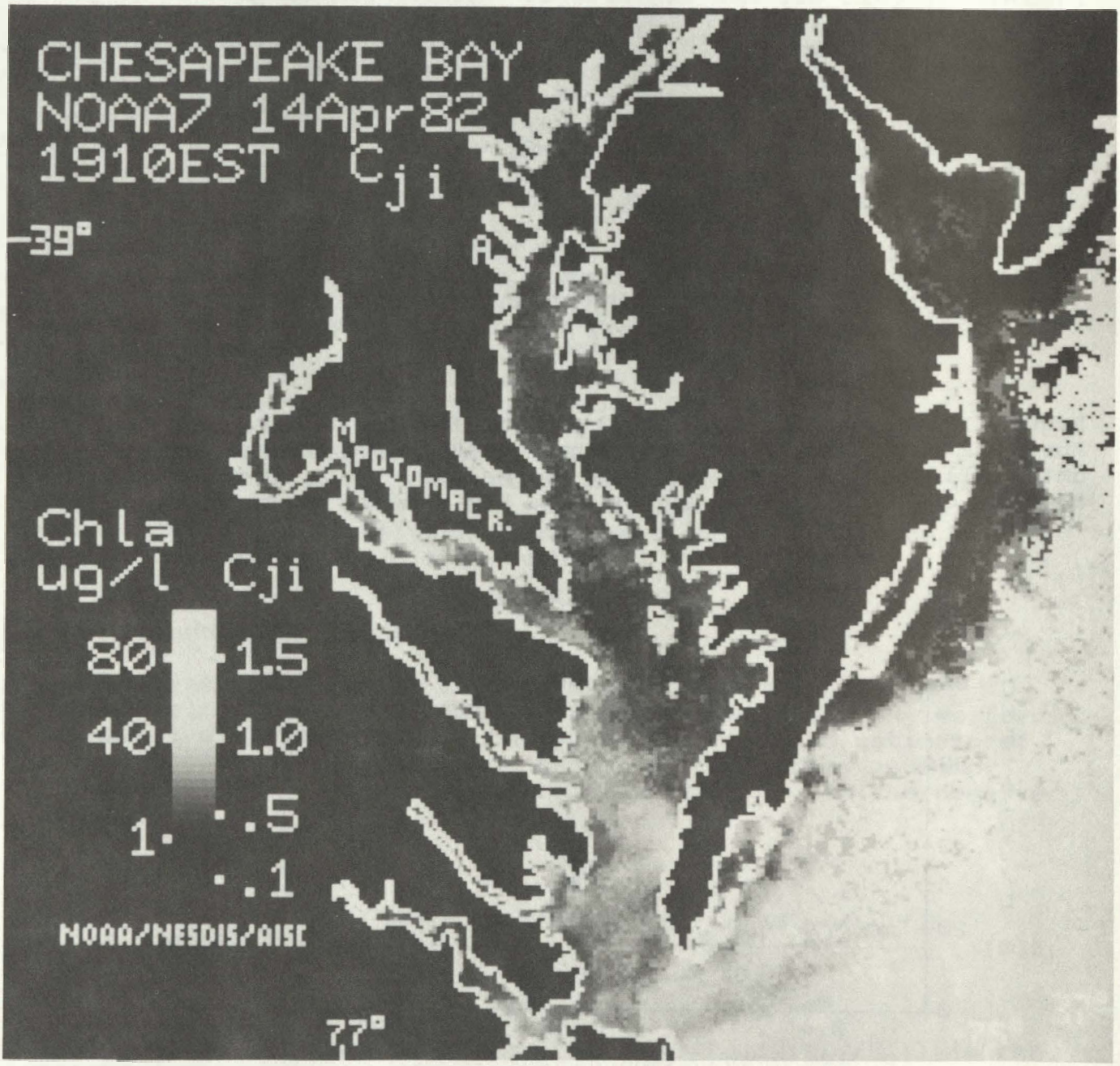

Figure 12: Chesapeake and Delaware Bays from NOAA-7 AVHRR, 14 April 1982, 1410 EST. A= Annapolis, M= Morgantown. a) R_T reflectance with estimated suspended sediment concentrations.

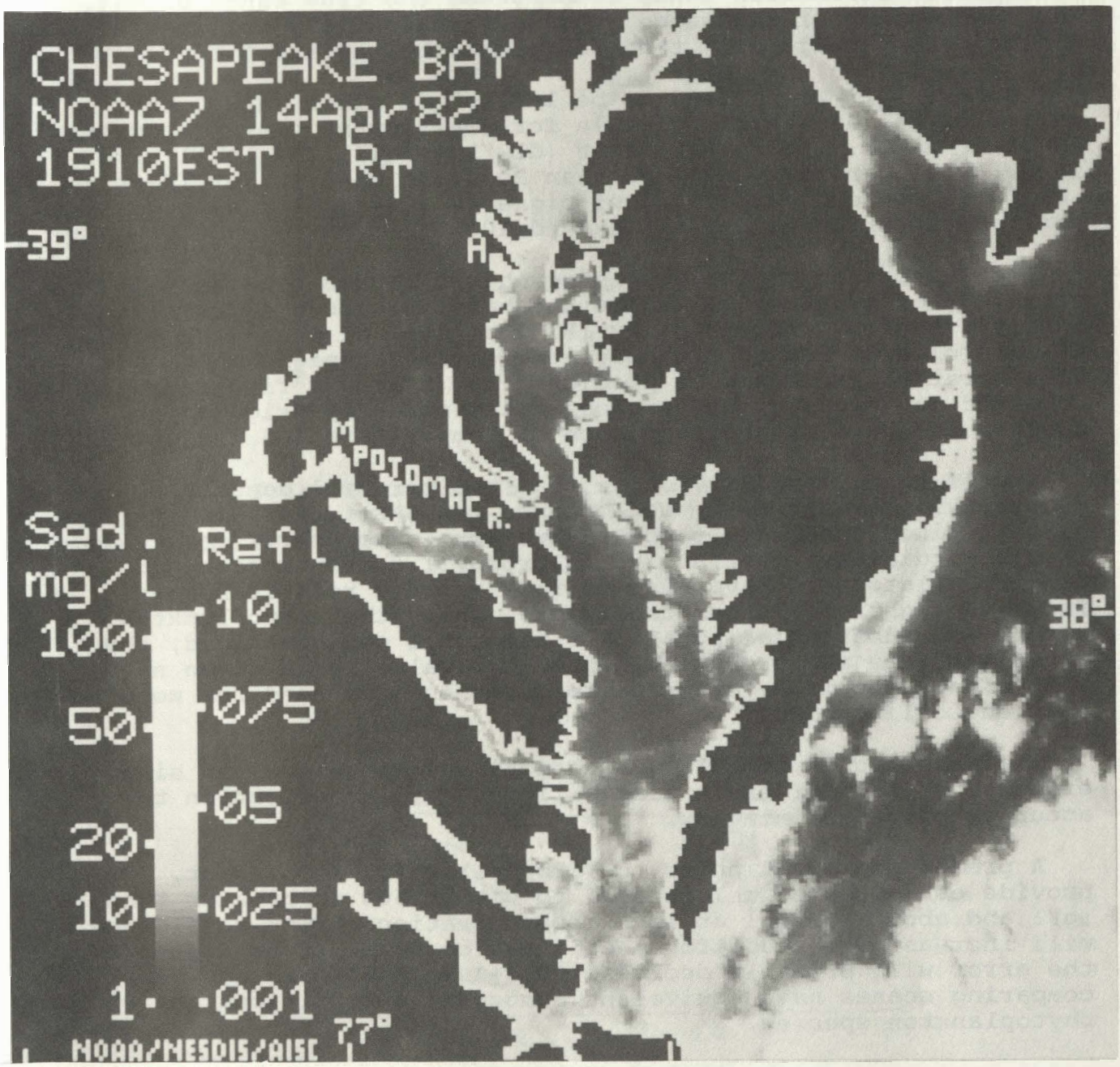

Figure 12b. C_{ji} and estimated chlorophyll-a on 14 April 1982.

Figure 13 shows the bias when L_A is not estimated exactly. The bias is fairly uniform for variations in C_{ji}, except when L_{Aj}' is too high, and typically will be less than 20-30%. In Figure 14 we see the result of local atmospheric error in C_{ji}: at low pigment concentrations, C_{ji} is overestimated, and at high pigment concentrations C_{ji} is underestimated. Thus this atmospheric correction tends to compress the true range of C_{ji}. The compression of the range by haze is physically reasonable; clouds, being white will tend to reduce the variation in color.

As dL_{Ai}/L_{wi}' would tend to be largest in clear water, the values of C_{ji} are least reliable for small quantities of pigments in clear water. In turbid water (dL_A/L_w small) the local error in C_{ji} will generally be less than 20%. In clear water ($R_T <$ .01) with low concentrations of pigments ($C_{ji}<.25$ or $n_c < 5$ µg/l), the error in C_{ji} can exceed 100%.

The distortion produced by atmospheric haze can be seen in the offshores of Figure 12b. Where the haze or clouds increase in density, thereby increasing R_T (Figure 12a), or where the water is very clear--such as offshore--the estimated pigment concentration increases as predicted by (5.6) and figure 14. Compared to water, clouds are characteristically brighter and cooler, and have greater variance in temperature and reflectance.

Stumpf and Tyler (1987) note that the per cell density of chlorophyll may alter the reflectance response. For example, certain dinoflagellates tend to have more chlorophyll per cell than some diatoms. For a give chlorophyll concentration, the dinoflagellate will have less surface area to reflect near-infrared light. In bloom conditions, where the phytoplankton comprise a substantial portion of the total sediment load, the dinoflagellate may produce a higher C_{ji} value for a given n_c. This effect should be examined to determine the need for more than one calibration.

The water color calculation effectively cancels grain size effects, so optical grain size will not have an effect on the accuracy of determining n_c.

A predefined equation for chlorophyll will, at present, provide estimates of chlorophyll to within 60% at greater than 10 µg/l and about $\pm$5 µg/l at lower concentrations. The confidence will increase with additional calibration data. From Figure 14, the error will probably decrease to $\leq\pm$30%, particularly when comparing scenes have equivalent atmospheric conditions and phytoplankton species.

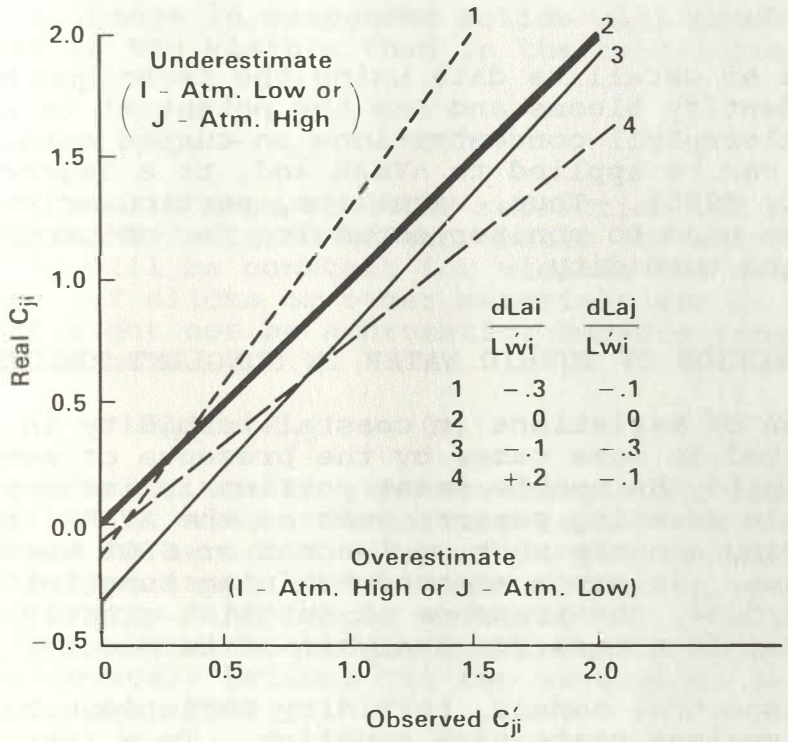

Figure 13: Scene bias showing difference between C_{ji} and C_{ji}' for different errors in dL_{Ai}/L_{wi}' and dL_{Aj}/L_{w1}' (atmospheric error normalized for assumed water radiance).

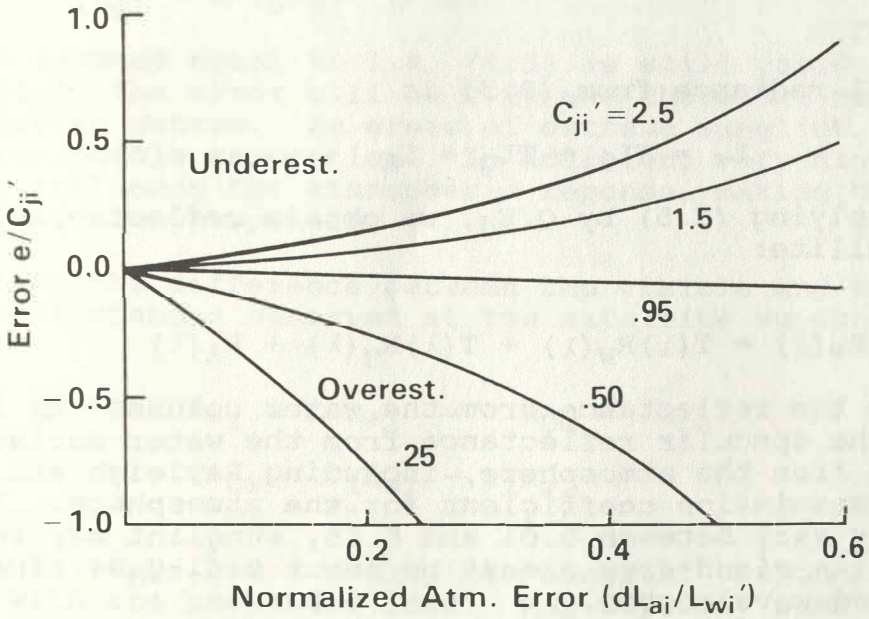

Figure 14: Local error in C_{ji} due to atmospheric contamination.

5.4. Conclusions.

The analysis of satellite data using the technique of vector analysis can identify blooms and has the potential to provide estimates of chlorophyll concentrations in turbid estuaries. This technique can be applied to AVHRR and, to a degree, with Landsat (Stumpf, 1985). Thus, satellite, particularly the AVHRR sensor, could be used to monitor estuaries for chlorophyll concentration and turbidity.

6. DETECTION OF TURBID WATER IN SUNGLINT REGIONS

The detection of variations in coastal turbidity in satellite imagery is limited in some cases by the presence of sunglint. The sunglint limits the usable scene portion in imagery obtained from a wide angle scanning sensor, such as the AVHRR, and also from nadir viewing sensors such as Landsat or SPOT when viewing tropical regions. As scene areas containing sunglint are otherwise cloud free, the presence of sunglint greatly reduces the number of usable scenes for analysis of turbidity.

With a multispectral sensor, turbidity variations can be extracted from regions containing sunglint. To a lesser degree, the same technique can eliminate some of the path radiance. Although not allowing for analysis of color variations with a two band sensor, the algorithm can allow some quantitative analysis of turbidity after the correction.

6.1. Theory

The total radiance from (3.5) is

$$L_* = TL_w + TL_g + L_A \qquad (3.5)$$

By multiplying (3.5) by Q/E_d, we obtain reflectance received at the satellite:

$$R_*(\lambda) = T(\lambda)R_w(\lambda) + T(\lambda)R_g(\lambda) + R_A(\lambda) \qquad (6.1)$$

where R_w is the reflectance from the water columns; R_g is the sunglint, the specular reflectance from the water surface; R_A is reflectance from the atmosphere, including Rayleigh and aerosol; T is the transmission coefficient for the atmosphere. In turbid water R_w may vary between 0.01 and 0.15, sunglint may reach 0.19, and R_a may (in cloud-free areas) be about 0.01-0.04 at red and near-infrared wavelengths.

The water column tends to strongly absorb near-infrared light and to reflect visible light. This difference in absorption

means that a change in suspended solids will cause R_w to change more rapidly in the visible than in the near-infrared. This can be written as

$$R_{w1} - R_{w2} > 0. \qquad (6.2)$$

Sunglint results from specular reflection off the water's surface. This reflectance is achromatic for water or sea water. Therefore, R_g will be constant for visible and near-infrared wavelengths. If slicks or other materials are on the surface, the sunglint might not be achromatic. Because sunglint is achromatic, we have

$$R_{g1} - R_{g2} = 0 \qquad (6.3)$$

The transmission varies with wavelength and atmospheric optical depth. It also incorporates losses due to Rayleigh scattering and to aerosols. Use of longer wavelength bands will minimize the importance of Rayleigh scattering and cause T to be roughly achromatic. At longer wavelengths, namely red and near-infrared light, we can consider the tranmission coefficient to vary proportionately between the two wavelength bands (Ahern et al., 1977; Griggs, 1983):

$$T_2 \simeq T_1/A \qquad (6.4)$$

with A between 0.9 and 1.0. Combining 6.3 and 6.4 gives

$$T_1R_{g1} - A\,T_2R_{g2} \simeq 0 \qquad (6.5).$$

If A is assumed equal to 1.0, (6.5) is still valid in most cases, because the error will be <.01 and therefore negligible for many turbid waters. In areas of extreme sunglint, (6.5) may not be a reasonable assumption. In addition, very high sunglint values may influence the atmospheric reponse, making the linear equation (6.1) inappropriate.

If we take the difference between the visible and near-infrared reflectances observed at the satellite we obtain

$$R_{D*} = R_{*1} - A\,R_{*2} = R_{Dw} + R_{DA} \qquad (6.6)$$

where

$$R_{Dw} = T_1R_{w1} - T_2R_{w2}$$
$$R_{DA} = R_{A1} - A\,R_{A2}.$$

The result, R_{D*}, has a negligible sunglint component. R_{Dw} will vary with the suspended load. R_{DA} may vary somewhat with the aerosol content. R_{DA} can be divided into Rayleigh and aerosol components. The Rayleigh reflectance can be calculated and therefore eliminated, if desired. In comparing different

scenes, performing some correction for atmospheric reflectance will be necessary because variations in R_{DA} will produce a bias in R_{D*}. If the scene can be corrected for R_A, the results is R_D.

Aerosol reflectance tends to be somewhat variable, although marine aerosols tend to have higher reflectance at near-infrared wavelengths than at visible wavelengths (Durkee, 1984). However, the differencing scheme, while not eliminating the aerosol component, will reduce it substantially (cf. the atmospheric correction performed by Gordon et al., 1983). The ratio R_{A1}/R_{A2} may vary between 1.3 and .7, depending on the aerosol type (Durkee, 1984). Then R_{DA} will be between 0.3 and -0.3 of R_{A1}.

6.2. Example Imagery

An image showing AVHRR reflectance (R_T) of the United States middle Atlantic appears in Figure 15. The image was taken at 1345 local time (EST) on 16 April 1982. The sun elevation was 36^o and the azimuth 226^o (SSW). Nadir in the scene lies at about 74^oW longitude. Therefore the inner shelf and estuaries lie in the region of maximum sunglint.

Sunglint characteristically varies with the wave steepness (Cox and Munk, 1954). In turn, wave steepness varies with wind speed at the surface and current speed, therefore we can expect variations in the glint pattern throughout the region. Glint is strongest in lower Chesapeake Bay, and offshore. Winds were from the southwest, hence the tendency for dark areas to appear in the lee of the land in Chesapeake Bay and off the North Carolina coast. Offshore, the variations in glint are due primarily to changes in wave heights resulting from changes in wind, and current strength and direction.

Figure 16 shows the scene after obtaining R_{D*}. Turbidity patterns have become evident and most of the sunglint pattern has been eliminated. The turbidity maxima at the heads of Chesapeake and Delaware Bays can now be seen, as can the clearer water in the lower bays and offshore. The difference in turbidity between between Pamlico Sound and offshore becomes quite apparent.

To verify the quality of the R_{D*} correction, we can compare Figure 16 with Figure 17, which shows a scene taken on 12 April 1982 that does not contain sunglint. The solar zenith angle for the second scene is 43^o and azimuth angle is 234^o. In this case the satellite is looking away from the sun. The turbidity variations indicated by Figure 16 compare favorably with those in Figure 17.

R_{D*} for 12 April appears in Figure 18. The close match between Figures 16 and 18 indicate the potential for calibration of the index.

Haze produces elevated values of R_T in figure 17. Much of the haze patterns have disappeared from figure 18, indicating the potential of this correction as an atmospheric correction. The variations in aerosol load that still exist are considerably less than in the combined reflectances (or the single channel data).

The difference between bands can be compared with suspended sediment concentrations (n_s) or turbidity indices (secchi depth or attenuation coefficient). As (4.3) applies to both bands, then the difference of R_{w1} and R_{w2} would also have that form:

$$R_{Dw} = m'\log(n_s) + b' \qquad (6.7)$$

with m' and b' constants for the new relationship.

Any analysis of R_{Dw} or calculation of n_s must consider possible variations in water color. Any pigment that decreases the reflectance in band 1 relative to band 2, even when the reflectance in <u>both</u> bands increases, will cause a decrease in R_{Dw}. Therefore, waters in which C_{ji} is high will tend to have lower R_{Dw}. Obviously, this caveat argues for the use of glint-free scenes in conjunction with the scenes containing glint in order to identify any major changes in water color. Comparisons of R_{Dw} can be made of any regions having comparable C_{ji}.

If R_{D*} is corrected for the atmosphere as described in chapter 3, we can use the corrected value R_D to approximate R_T:

$$R_T = g\ R_D \qquad (6.8)$$

where

$$g = \frac{(E_{o1} + C_{ji}E_{o2})}{(E_{o1} + E_{o2})(1-C_{ji})}$$

For the AVHRR, when C_{ji}=0.28, then R_T= R_D. However, as C_{ji} increases, the value of g increases. For C_{ji}>0.28, we find R_T>R_D. Also, if C_{ji}>1, R_D becomes negative. As a result, turbid water with high C_{ji} may have a smaller R_D than clearer water with low C_{ji}. Possibly setting $g = 1/C_{ji}^{b}$, with b a constant, may provide a simpler approximation to obtain R_T from R_D.

6.3. Additional Applications

For different sensors, sunglint "removal" would be most effective with red and near-infrared bands. Besides AVHRR bands 1 and 2, these would include Landsat MSS (multispectral scanner) bands 5 (500-600 nm) and 6 (600-700 nm), Landsat Thematic Mapper

bands 3 (630-690 nm) and 4 (760-900 nm), and SPOT bands 2 (610-680 nm) and 3 (790-890 nm). Because this algorithm depends on maximum differences between the visible and near-infrared bands, materials that reduce this difference would make it less effective. For example, chlorophyll-like pigments absorb red light. When chlorophyll concentration exceeds about 30-40 g/l, the AVHRR infrared band may have the same or greater reflectance than the visible band (Stumpf and Tyler, 1987). Similar effects may occur under very high sediment loads with a high iron content or where R in the visible band has reached its asymptotic value. Therefore, calibration of the R_{Dw} with n_s will require knowledge of the water color.

This technique can be used for both aerial sensors and spacecraft sensors. The differencing scheme will provide some correction for atmosphere and, for most cases where the logarithmic relationship applies between R_{Dw} and n_s, it can be used between R_{Dw} and n_s.

7. CONCLUSIONS

The AVHRR has three strengths in estuarine and coastal studies: frequent sampling, repetitive imagery, and a wide viewing area. As a result the AVHRR can permit study of events occurring on daily to seasonal scales, and allow regional comparisons of estuaries and associated coastal waters.

The ability to produce consistent estimates of temperature and sediment and chlorophyll concentration using satellite will enhance estuarine and coastal research. The logistical restraints of sampling from ship have limited the study of episodic events, spatial variability, and the development of models. Modeling, in particular, requires synoptic detail that cannot be provided by ship. Although satellites cannot provide data on the subsurface, the AVHRR can provide frequent synoptic coverage of surface distributions suitable for initializing and verifying model results.

The wide field of view of the AVHRR simplies study of large estuaries because one scene can cover the entire region. On the other hand, because of its limited resolution, the AVHRR cannot help oceanographers who are studying very small estuaries (<12 km^2). But the design of the algorithms presented here allow for their application to Landsat or SPOT, or aircraft-mounted sensors. Therefore, information can be acquired in smaller estuaries and compared with the data from the region, or from other estuaries.

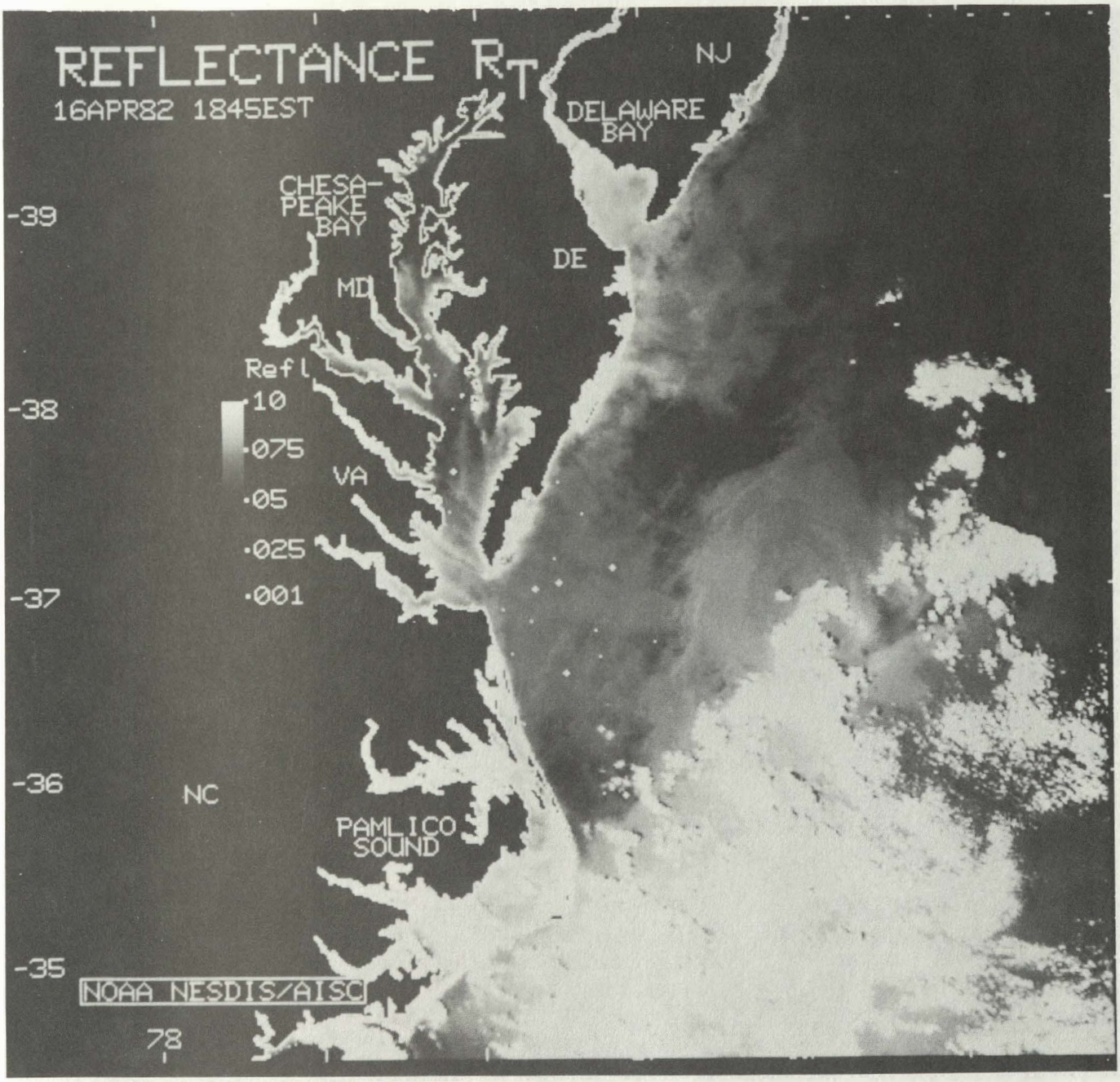

Figure 15: Approximate R_T from NOAA-7 AVHRR for the U.S. Mid-Atlantic Bight, 16 April 1982.

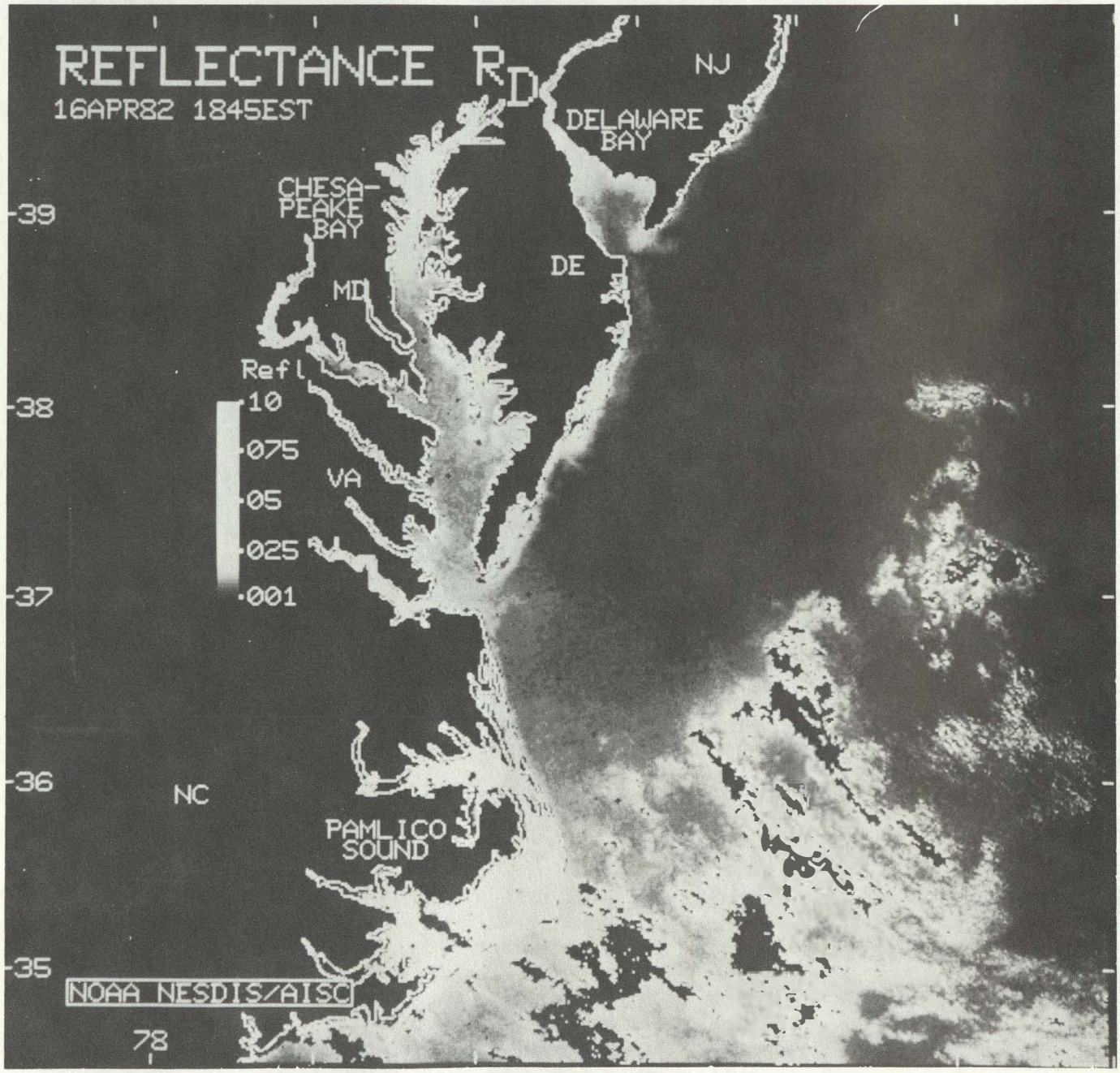

Figure 16: R_D reflectance for same scene as figure 15 (16 April 1982).

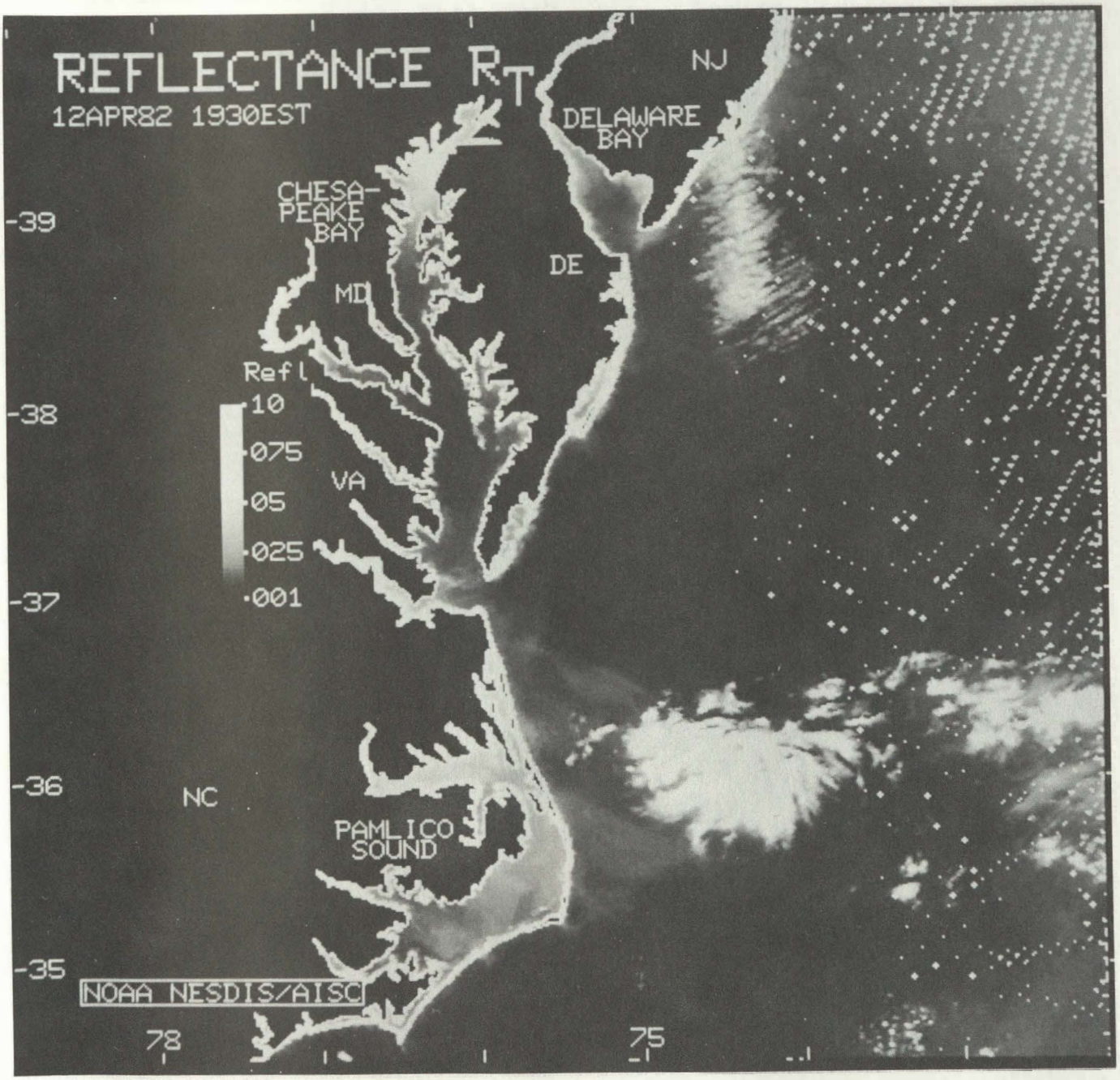

Figure 17: R_T reflectance from NOAA-7 AVHRR for the U.S. Mid-Atlantic Bight, 12 April 1982.

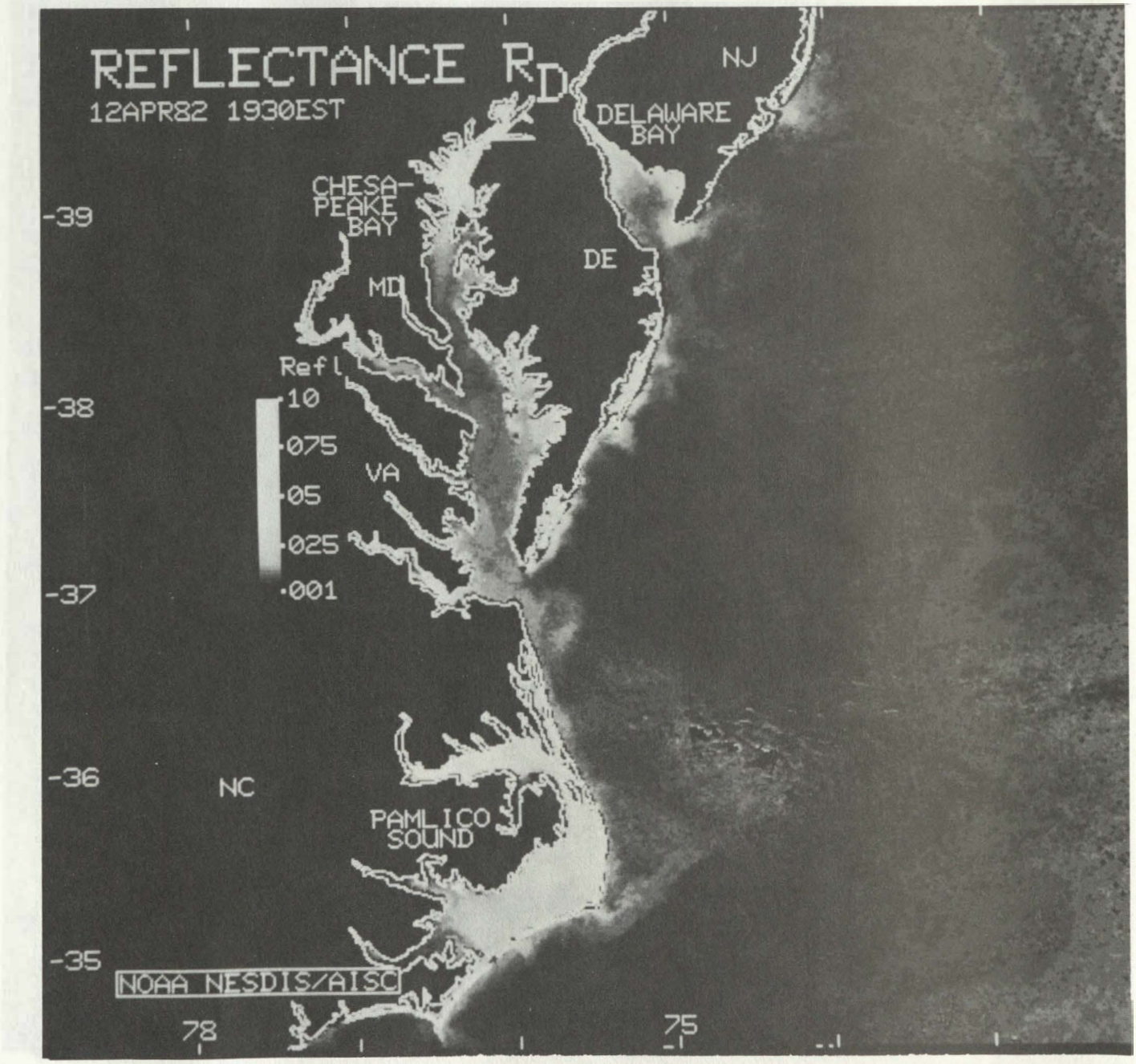

Figure 18: R_D reflectance for the same scene as Figure 17 (12 April 1982).

8. REFERENCES

Ahern, F.J., D.G. Goodenough, S.C. Jain, and V.R. Rao, 1977: Use of clear lakes as standard reflectors for atmospheric measurements. Proc. 11th Intl. Symp. Remote Sensing of Environment, ERIM, Ann Arbor, Michigan, Vol1, p. 731-755.

Aranuvachapun, S. and P.H. LeBlond, 1981: Turbidity of coastal waters determined from Landsat. Remote sensing of Environment, 84:113-132.

Austin, R., 1974: The remote sensing of spectral radiance from below the ocean surface. in: Jerlov, N.G. and Nielson, B., eds., Optical Aspects of Oceanography, Academic Press, New York, p. 317-345.

Austin, R., 1979: Coastal zone color scanner radiometry. Society Photo-Optical Instrumentation Engrs. vol 208 (Ocean Optics VI):170-177.

Born, G.H., C. Wunsch, and C.A. Yamarone, 1984: TOPEX, Observing the oceans from space. Eos, 65(28):433-434.

Bowker, D.E., W.G. Witte, P. Fleischer, T.A. Gosink, W.J. Hanna, and J.C. Ludwick, 1975: An investigation of the waters in the lower Chesapeake Bay area. 10th Intl. Symp. on Remote Sensing of Environment, ERIM, Ann Arbor, Michigan, p.411-420.

Bukata, R.P., J.H. Jerome, J.E. Bruton, S.C. Jain, H.H. Zwick, 1981: Optical water quality model of Lake Ontario I: Determination of the optical cross sections of organic and inorganic particulates in Lake Ontario. Applied Optics, 20:1696-1703.

Catts, G.P., S. Khorram, J.E. Cloern, A.W. Knight, and S.D. DeGloria, 1985: Remote sensing of tidal chlorophyll-a variations in estuaries. Intl. Journal of Remote Sensing, 6:1685-1705.

Cox, C.C. and W. Munk, 1954: Measurement of the roughness of the sea surface from photographs of the sun's glitter. Journal, Optical Society of America, 44:838-850.

Duntley, S.Q., R.W. Austin, W.H. Wilson, C.F. Edgerton, S.E. Moran, 1974: Ocean Color Analysis. SIO ref 74-10, Scripps Institute of Oceanography, University of California, San Diego.

Durkee, P.A., 1984: The Relationship between Marine Aerosol Particles and Satellite-Detected Radiance. Colorado State Univ. Ph.D. diss. Atmospheric Science Paper #380, 124 p.

Durkee, P.A., D.R. Jensen, E.E. Hindman, and T.H. Vander Haar, 1986: The relationship between marine aerosol particles and satellite-detected radiance. Jour. Geophysical Research, 91(D3):4063-4072.

Everdale, F., 1986: Satellite Oceanography - Volume I: NOAA-n AVHRR Digital Data. Natl. Oceanographic and Atmospheric Admin., Assessment and Information Services Center, Washington, DC, 63 p.

Gagliardini, D.A., H. Karszenbaum, R. Legeckis, and V. Klemas, 1984: Application of Landsat MSS, NOAA/TIROS AVHRR, and Nimbus CZCS to study the La Plata River and its interaction with the ocean. Remote Sensing of Environment, 15:21-36.

Gordon, H.R., 1978: Removal of atmospheric effects from satellite imagery of the oceans. Applied Optics, 17:1631-1636.

Gordon, H.R. and A.Y. Morel, 1983: Remote Assessment of Ocean Color for Interpretation of Satellite Visible Imagery. A Review. Lecture Notes on Coastal and Estuarine Studies, Springer-Verlag, New York.

Gordon, H.R. O.B. Brown, and M.M. Jacobs, 1975: Computed relationships between the inherent and apparent optical properties of a flat homogeneous ocean. Applied Optics, 14:417-427.

Gordon, H.R., D.K. Clark, J.W. Brown, O.B. Brown, R.H. Evans, and W.W. Broenkow, 1983: Phytoplankton pigment concentrations in the Middle Atlantic Bight: comparison of ship determinations and CZCS estimates. Applied Optics, 22:20-33.

Griggs, M., 1983: Satellite measurements of tropospheric aerosols. Advances in Space Research, 2:109-118.

Jain, S.C., and J.R. Miller, 1977: Algebraic expression for the diffuse irradiance reflectivity of water from the two flow model. Applied Optics, 16:202-204.

Jerlov, N.G., 1976: Marine Optics, Elsevier, New York, 231 p.

Kidwell, K.B., 1984: NOAA Polar Orbiter Data (TIROS-N, NOAA-6, NOAA-7, NOAA-8, NOAA-9) Users Guide, revised May 1985, Natl. Oceanographic and Atmospheric Admin., Natl. Environmental Satellite Data and Information Service, Washington DC.

Klemas, V., M. Otley, W. Philpot, C. Wethe, R. Rogers, and N. Shah, 1974: Correlation of coastal water turbidity and circulation with ERTS-1 and Skylab imagery. 9th Intl. Symp. on Remote Sensing of Environment, Ann Arbor, Mich., p. 1289-1317.

Klemas, V. and W.D. Philpot, 1983: Drift and dispersion studies of ocean dumped waste using Landsat imagery and current drogues. Photogr. Engr. and Remote Sensing, 47:533-542.

Lauritson, L., G.J. Nelson, and F.W. Porto, 1979: DAta Extraction and Calibration of TIROS-N/NOAA Radiometers, National Oceanic and Atmospheric Administratin, Washington, D.C., Technical Memo. NESS 107, with admendments.

McMillan, L.M. and D.S. Crosby, 1984: Theory and validation of the multiple window sea surface temperature technique. Jour. Geophysical Research, 89(C3):3655-3661.

Moore, G.K., 1980: Satellite remote sensing of water turbidity. Bull. Hydrological Sciences, 25:407-421.

Morel, A. and L. Prieur, 1977: Analysis of variations in ocean color. Limnology and Oceanography, 22:709-722.

Munday, J.C. and M.S. Fedosh, 1981: Chesapeake Bay plume dynamics from Landat. in (J.W. Campbell and J.P. Thomas, eds.) Superflux: Chesapeake Bay Plume Study. NASA Conference Publ. 2188.

Munday, J.C. and T.T. Alfoldi, 1979: LANDSAT test of diffuse reflectance models for aquatic suspended solids measurements. Remote Sensing of Environment, 8:169-183.

Neckel, H. and D. Labs, 1981: Improved data of solar spectral irradiance from 0.33 to 1.25 m. Solar Physics, 74:231-249.

Philpot, W.D., 1981: A Radiative Transfer Model for Remote Sensing of Vertically Inhomogeneous Waters. Univ. Delaware Ph.D. Diss., 140 p.

Postma, H., 1961: Suspended matter and Secchi disc visibility in coastal waters. Netherlands Jour. Sea Research, 1:359-390.

Preisendorfer, R.W., 1976: Hydrologic Optics, U.S. Dept. of Commerce, NOAA, USGPO 76-677-881/36, volume I.

Prieur, L. and S. Sathyendranath, 1981: An optical classification of coastal and oceanic waters based on the specific spectral absorption curves of phytoplankton pigments, dissolved organic matter and other particulate materials. Limnology and Oceanography, 26:671-689.

Singh, S.M. and A.P. Cracknell, 1986: The estimation of atmospheric effects for SPOT using AVHRR channel-1 data. Intl. Journal of Remote Sensing, 7:361-377.

Smith, R.C. and K.S. Baker, 1978: Optical classification of natural waters. Limnology and Oceanography, 23(2):260-267.

Smith, R.C. and K.S. Baker, 1981: Optical properties of the clearest natural waters (200-800nm). Applied Optics, 20:177-184.

Strong, A.E. and E.P. McClain, 1984: Improved ocean surface temperatures from space--comparisons with drifting buoys. Bull. American Meteorological Society, 65:138-142.

Stumpf, R.P., 1985: Physical interpretation of estuarine water color using vector analysis of satellite data. in (K.R. Carver, ed.) Digest of Intl. Geophysical and Remote Sensing Symposium (IGARSS), Inst. Electrical Electronics Engrs., New York, p. 970-976.

Stumpf, R.P, 1987: Sediment transport in Chesapeake Bay during floods: analysis using satellite and surface observations. submitted to Journal of Coastal Research.

Stumpf, R.P. and M.A. Tyler, 1987: Satellite detection of bloom and pigment distributions in estuaries. (in prep.).

Sturm, B., 1981: Ocean colour remote sensing and quantitative retrieval of surface chlorophyll in coastal waters using Nimbus CZCS data. in J.F. R. Gower (ed.) Oceanography from Space, Plenum Press.

Tassan, S. and B. Sturm, 1986: An algorithm for the retrieval of sediment content in turbid coastal waters from CZCS. Intl. Jour. Remote Sensing, 7(5):643-655.

Tyler, M.A. and R.P. Stumpf, 1987: Feasibility of using satellite for detection and kinetics of small scale phytoplankton blooms in estuaries. tidal and migration effects. (in prep.).

Van de Hulst, H.C., 1957: Light Scattering by Small Particles. John Wiley and Sons, New York.

Whitlock, C.H., L.R. Poole, J.W. Usry, W.M. Houghton, W.G. Witte, W.D. Morris, and E.A. Gurganus, 1981: Comparison of reflectance with backscatter and absorption parameters for turbid waters. Applied Optics, 20(3):517-527.

Witte, W.G., C.H. Whitlock, R.C. Harriss, J.W. Usry, L.R. Poole, W.M. Houghton, W.D. Morris, and E.A. Gurganus, 1982: Influence of dissolved organic materials on turbid water optical properties and remote sensing reflectance. Jour. Geophysical Research, 87(C1):441-446.

APPENDIX A.
DETERMINING REFLECTANCE OR COLOR ON EASI/PACE

The EASI procedure REFLECT4 will determine R_T, del R_*, or C_{ji} from input AVHRR channel 1 and 2 raw count value data. The file containing the channel 1 and 2 images must have one available file for each resultant image. The output is scaled such that 1 count = .001 R_T, .001 del R_*, or 0.1 C_{ji}.

Prior to running this program, the user must have determined L_{ac} for both channels. The user must also have the central latitude and longitude for the image, the Julian Date, and the GMT for the image.

To operate type

```
RUN REFLECT4
```

A sample run follows with input values underlined

```
REFLECT CALCULATES EITHER REFLECTANCE OR COLOR (CJI)
FROM AVHRR CHANNELS 1 AND 2
REFLECTANCE MAY BE DIFFERENCE OR COMBINED TOTAL
USER MUST HAVE ATMOSPHERIC CORRECTION
JULIAN DATE, GMT, AND IMAGE LATITUDE AND LONGITUDE
REFLECTANCE OUTPUT IS SCALED 0-25.5% = 0-255 COUNTS
COLOR (CJI) IS SCALED 0-2.55 = 0-255 COUNTS

PARAMETER SCENE CONTAINS
       (1) JULIAN DATE
       (2) GMT
       (3) CENTER LATITUDE AND
       (4) CENTER LONGITUDE, WEST IS NEGATIVE

SCENE - SCENE DATE,GMT,LAT,LONG    >    102    1929    38    -76

CORRECT VALUES? (Y OR N)> N

SCENE - SCENE DATE,GMT,LAT,LONG    >100,1900,38,-76

                  (Enter scene Julian date,GMT,latitude
                   and longitude as shown)

SCENE - SCENE DATE,GMT,LAT,LONG    >    100    1900    38    -76

CORRECT VALUES? (Y OR N)> Y


***SOLAR ZENITH ANGLE = 39.7941  DEGREES  ***
***SOLAR AZIMUTH ANGLE = 208.69  DEGREES  ***
***EARTH ORBITAL RADIUS CORRECTION = 0.99670
```

```
NOAA SATELLITE NUMBER> 9              (program works for NOAA 6-10)

FILENAME >FILENAME
CHANNEL 1 AND CHANNEL 2 IMAGE # >1,2
CHANNEL 1 ATM.CORR IN COUNTS >60
CHANNEL 2 ATM.CORR IN COUNTS >48
ATM.CORRECTION, CH.1, CH.2= 60  48
CORRECT? Y OR N > Y

CORRECT FOR ATMOS. ATTEN. > Y        (If you do not wish to correct
                                      for T, type N)

ATM1,ATM2,AER1,AER2,TRAN1,TRAN2
     60     48    1.26536 0.41656 0.84835 0.91288
```

(The above printout gives the atmospheric correction in counts--ATM1,ATM2=60,48; in radiance--AER1,AER2=1.26536,0.41656; and T for both bands--TRAN1,TRAN2=0.84835,0.91288)

```
OUTPUT IMAGE # >4

CHOOSE REFLECTANCE DIFFERENCE (D), TOTAL (T)
OR COLOR (C) >D
```

(At this point you will see the PACE routine status and a start time. Upon completion, a finish time will appear and the procedure will continue with:)

```
ANOTHER CORRECTION FOR THIS SCENE? Y OR N > Y
```

(if you enter N the program will end at this time)

```
SAME ATMOSPHERIC CORRECTION?  Y OR N > Y
```

(if you answer N the program will repeat with the prompt "CHANNEL 1 ATM.CORR IN COUNTS >". If you answer Y it continues with verification of the atmospheric correction, then the request for the output image #.)

The program will take about 45 seconds per correction on the VAX 11/780 and 3-4 minutes on the IBM PC/AT.

ERRATA

p.5, section 3.1, line 13 should read:
$E_o = \underline{E}_o/\{1-0.0167 \cos[2\pi(D-3)/365]\}^2$

p.8, section 3.3, par.2, line 6 should read: "1000-2000 nm."

p.12, table 4, column 1 and footnote: E_{o1} and E_{o2} should read $\underline{E}_{o1}$ and $\underline{E}_{o2}$, respectively

p.16, section 4.3, line 12 and line 17 insert ρ:
". . where ρ is the particle density."
". . same fashion with (ρd)."

p.30, par.1, line 10 should read: "(R_T > 0.07)"

p.30, par.2, line 2 should read: "R_T up to 0.07"

p.40, line 6, insert μ: "30-40 μg/l"

p.47, Neckel and Labs reference insert μ: "0.33 to 1.25 μm"